Agricultural and Forest Meteorology 242 (2017) 55–74

Contents lists available at ScienceDirect

Agricultural and Forest Meteorology

journal homepage: www.elsevier.com/locate/agrformet

Research Paper

Improving global terrestrial evapotranspiration estimation using support vector machine by integrating three process-based algorithms

Yunjun Yao[a,*], Shunlin Liang[a], Xianglan Li[b], Jiquan Chen[c], Shaomin Liu[d], Kun Jia[a], Xiaotong Zhang[a], Zhiqiang Xiao[a], Joshua B. Fisher[e], Qiaozhen Mu[f], Ming Pan[g], Meng Liu[h,i], Jie Cheng[a], Bo Jiang[a], Xianhong Xie[a], Thomas Grünwald[j], Christian Bernhofer[j], Olivier Roupsard[k,l]

[a] *State Key Laboratory of Remote Sensing Science, Institute of Remote Sensing Science and Engineering, Faculty of Geographical Science, Beijing Normal University, Beijing, 100875, China*
[b] *College of Global Change and Earth System Science, Beijing Normal University, Beijing, 100875, China*
[c] *CGCEO/Geography, Michigan State University, East Lansing, MI 48823, USA*
[d] *State Key Laboratory of Earth Surface Processes and Resource Ecology, School of Natural Resources, Faculty of Geographical Science, Beijing Normal University, Beijing, 100875, China*
[e] *Jet Propulsion Laboratory, California Institute of Technology, 4800 Oak Grove Dr., Pasadena, CA 91109, USA*
[f] *Numerical Terradynamic Simulation Group, Department of Ecosystem and Conservation Sciences, University of Montana, Missoula, MT 59812, USA*
[g] *Department of Civil and Environmental Engineering, Princeton University, Princeton, New Jersey, NJ 08544, USA*
[h] *Institute of Geographic Sciences and Natural Resources Research, Chinese Academy of Sciences, Beijing 100101, China*
[i] *University of Chinese Academy of Sciences, Beijing 100049, China*
[j] *Technische Universität Dresden, Institute of Hydrology and Meteorology, Chair of Meteorology, 01062 Dresden, Germany*
[k] *CIRAD, UMR Eco & Sols (Ecologie Fonctionnelle & Biogéochimie des Sols et des Agro-écosystèmes), 34060 Montpellier, France*
[l] *CATIE (Tropical Agricultural Centre for Research and Higher Education), 7170 Turrialba, Costa Rica*

ARTICLE INFO

Keywords:
Terrestrial evapotranspiration
Machine learning methods
Bayesian model averaging method
Plant functional type

ABSTRACT

Terrestrial evapotranspiration (*ET*) for each plant functional type (*PFT*) is a key variable for linking the energy, water and carbon cycles of the atmosphere, hydrosphere and biosphere. Process-based algorithms have been widely used to estimate global terrestrial *ET*, yet each *ET* individual algorithm has exhibited large uncertainties. In this study, the support vector machine (*SVM*) method was introduced to improve global terrestrial *ET* estimation by integrating three process-based *ET* algorithms: *MOD16*, *PT-JPL* and *SEMI-PM*. At 200 *FLUXNET* flux tower sites, we evaluated the performance of the *SVM* method and others, including the Bayesian model averaging (*BMA*) method and the general regression neural networks (*GRNNs*) method together with three process-based *ET* algorithms. We found that the *SVM* method was superior to all other methods we evaluated. The validation results showed that compared with the individual algorithms, the *SVM* method driven by tower-specific (Modern Era Retrospective Analysis for Research and Applications, *MERRA*) meteorological data reduced the root mean square error (*RMSE*) by approximately 0.20 (0.15) mm/day for most forest sites and 0.30 (0.20) mm/day for most crop and grass sites and improved the squared correlation coefficient (R^2) by approximately 0.10 (0.08) (95% confidence) for most flux tower sites. The water balance of basins and the global terrestrial *ET* calculation analysis also demonstrated that the regional and global estimates of the *SVM*-merged *ET* were reliable. The *SVM* method provides a powerful tool for improving global *ET* estimation to characterize the long-term spatiotemporal variations of the global terrestrial water budget.

1. Introduction

Evapotranspiration (*ET*), the sum of evaporation from the Earth's surface and transpiration from plants into the atmosphere, is an important variable linking the global terrestrial water, carbon and energy exchanges (Allen et al., 1998; Liang et al., 2010; Wang and Dickinson, 2012). In general, *ET* returns approximately 60% of precipitation onto the Earth's surface back to the atmosphere (Korzoun et al., 1978) and thereby conveys terrestrial water availability at the global scale (Mu et al., 2011; Yao et al., 2015). An accurate

* Corresponding author.
E-mail address: boyyunjun@163.com (Y. Yao).

http://dx.doi.org/10.1016/j.agrformet.2017.04.011
Received 26 October 2016; Received in revised form 16 February 2017; Accepted 12 April 2017

estimation of terrestrial *ET* is crucial to understand the linkages between the terrestrial water budget and climate change. However, regional *ET* is inherently difficult to measure because of the heterogeneity in the landscape and the large number of complex controlling biophysical processes, such as available energy, plant biophysics and soil moisture (Friedl, 1996; Mu et al., 2007; National Research Council, 2007; Jiménez et al., 2011).

Remote sensing provides us broad spatial coverage and regular temporal sampling of biophysical parameters (*e.g.* vegetation indices, *VIs*, albedo, leaf area index, *LAI*, fraction of absorbed photosynthetically active radiation, *FPAR*, land surface temperature, *LST*, and plant functional types, *PFTs*) (Liang et al., 2013; Los et al., 2000; Yao et al., 2013) for estimating regional *ET*. Over the past several years, many satellite-based methods were designed and developed to estimate regional *ET*, including (1) physically-based algorithms (Allen et al., 2007; Bastiaanssen et al., 1998; Fisher et al., 2008; Kustas and Daughtry, 1990; Mu et al., 2007; Norman et al., 1995; Priestley and Taylor, 1972); (2) data assimilation (*DA*) methods (Pipunic et al., 2008; Xu et al., 2011a,b) and (3) empirical/semi-empirical algorithms (Jackson et al., 1977; Wang et al., 2007; Wang and Liang, 2008; Wang et al., 2010a,b; Yao et al., 2015). Traditional physically-based algorithms, such as Surface Energy Balance System (*SEBS*) (Su, 2002), the Surface Energy Balance Algorithm for Land (*SEBAL*) algorithm (Bastiaanssen et al., 1998), the Two-Source *ET* model coupled with Atmosphere-Land Exchange Inverse (*ALEXI*) model (Anderson et al., 1997), the Moderate Resolution Imaging Spectroradiometer (*MODIS*) *LAI*-based Penman-Monteith (*PM*) equation (Mu et al., 2007; Mu et al., 2011) and Priestley-Taylor (*PT*) algorithm (Priestley and Taylor, 1972; Fisher et al., 2008), model the dynamics of *ET* process based on surface energy balance (*SEB*) equation and the Monin-Obukhov Similarity Theory (*MOST*) driven by satellite and meteorological observations (Wang and Dickinson, 2012). However, their simulation results may differ substantially due to the large errors from too many input variables and uncertainty that exists in the structures of the models. Although *DA* methods assimilate satellite-based parameters (e.g., *LAI*, *LST*) into biophysical or land surface models (*LSMs*) to improve *ET* estimation (Pipunic et al., 2008; Xu et al., 2011a,b), a longstanding limitation associated with *DA* methods is that the *ET* simulation accuracy has been mainly affected by the accuracy of satellite-based input variables.

Empirical/semi-empirical algorithms have been developed by relating ground-measured *ET* to satellite-based vegetation parameters and other key meteorological variables (Wang et al., 2007). As specific empirical algorithms, data-driven methods, including artificial neural network (*ANN*) (Lu and Zhuang, 2010), support vector machine (*SVM*) (Shrestha and Shukla, 2015; Yang, 2006) and model tree ensembles (*MTE*) (Jung et al., 2010) estimate *ET* by building relationships between input variables and outputs (*ET*) using training datasets. These methods are sound in theory and provide accurate estimates of *ET* as long as enough training datasets are representative of all the behaviors found in the systems. However, they still show substantial differences in partitioning *ET* for different regions and biomes due to the limited training data at certain sites. Moreover, large data requirements for data-driven methods can reduce their computational efficiency for generating satellite-based *ET* products.

Multi-model ensemble approaches have been successfully used to improve global terrestrial *ET* estimation. Former studies have indicated that a simple model averaging method (*SMA*) or Bayesian model averaging (*BMA*) method is superior to single model for predicting terrestrial latent heat flux (*LE*) and surface longwave radiation (Chen et al., 2015; Wu et al., 2012; Yao et al., 2014). For example, Yao et al. (2014) used the *BMA* method to merge five process-based *LE* algorithms and effectively improved the skills of the algorithms. Wu et al. (2012) also found that the *BMA* method has the highest accuracy than individual algorithms to combine eight land surface long-wave radiation algorithms. These multi-model ensemble approaches obtain more accurate estimates of the surface energy budget based on the linear combination of each single model by gathering useful information from multiple models to produce ensemble predictions. In theory, multi-model ensemble approaches based on a nonlinear combination of each single model, such as machine learning techniques, performs better than those based on a linear combination of each single model (*e.g. BMA* method) for predicting hydrologic and biophysical variables (Duan and Phillips, 2010; Sheffield and Wood, 2008). However, there is a lack of similar studies on predicting global terrestrial *ET* using machine learning methods for merging multi-models.

In this paper, to reduce uncertainties in global *ET* estimation using the individual process-based *ET* algorithms, we used the classical machine learning method, the *SVM* method, to improve global terrestrial *ET* estimation by merging three process-based algorithms. In Yao et al., 2014 paper, five *ET* algorithms including two *PM* algorithms, two *PT* algorithms and one semi-empirical Penman algorithm were merged for *ET* estimation. However, numerous studies found the similar performance of above two *PM* or *PT* algorithms for most land cover types (Yao et al., 2014; Yuan et al., 2010). Therefore, in this study, we only selected one *PM* algorithm, one *PT* algorithm and one semi-empirical Penman algorithm for *ET* estimation. Our specific objectives are to: 1) assess the performance of the *SVM* method for merging three process-based *ET* algorithms based on a series of cross-validations using long-term *FLUXNET* eddy covariance (*EC*) observations from 2000 through 2009; 2) compare the *SVM* method with the *BMA* method, the general regression neural networks (*GRNNs*) method and the water balance (*WB*) equation at the site and basin scales; and 3) generate a global daily *ET* product during 2003–2005 with well-quantified accuracy based on *MODIS* data and Modern Era Retrospective Analysis for Research and Applications (*MERRA*) meteorological data.

2. Data and methods

2.1. Data source

2.1.1. Data at eddy covariance flux tower sites

The performances of the *SVM* method, the *GRNNs* method, the *BMA* method and three process-based *ET* algorithms were examined using ground-measured *EC* data. The data were collected at 200 *EC* flux tower sites located in Asia, Europe, Africa, Australia, South America and North America (Fig. 1). The data were collected from AsiaFlux, AmeriFlux, LathuileFlux, Arid/Semi-arid experimental observation synergy and integration, the Chinese Ecosystem Research Network (*CERN*) and some individual principal investigators (*PIs*) of the *FLUXNET* project. The *EC* flux tower sites included nine major biomes: evergreen broadleaf forests (*EBF*, 14 sites), evergreen needleleaf forests (*ENF*, 50 sites), deciduous broadleaf forests (*DBF*, 24 sites), deciduous needleleaf forests (*DNF*, 4 sites), mixed forests (*MF*, 10 sites), shrubland (*SHR*, 12 sites), savanna (*SAW*, 8 sites), croplands (*CRO*, 30 sites) and grasslands and other types (*GRA*, 48 sites). The data included half-hourly or hourly surface net radiation (R_n), solar radiation (R_s), soil heat flux (G), air temperature (T_a), vapor pressure (e), maximum air temperature ($T_{\max}$), relative humidity (RH), wind speed (WS), sensible heat flux (H) and ET. Half-hour *EC* measurements were obtained from the raw data sampled at 10 Hz with the post-processing software EdiRe (University of Edinburgh, http://www.geos.ed.ac.uk/abs/research/micromet/EdiRe). When the number (N) of half-hourly measurements exceeded 40 per day, the daily average R_n, R_s, G, T_a, e, $T_{\max}$, RH, WS, H and ET were the averages of the measurements. Thus, the total daily ET can be calculated as:

$$ET = \frac{1}{N}\sum_{i=1}^{N} ET_i \times 48 \tag{1}$$

Where i is the ith half-hourly observation on each day. If N was less than 40, the daily measurements were set to a fill value. Otherwise, they

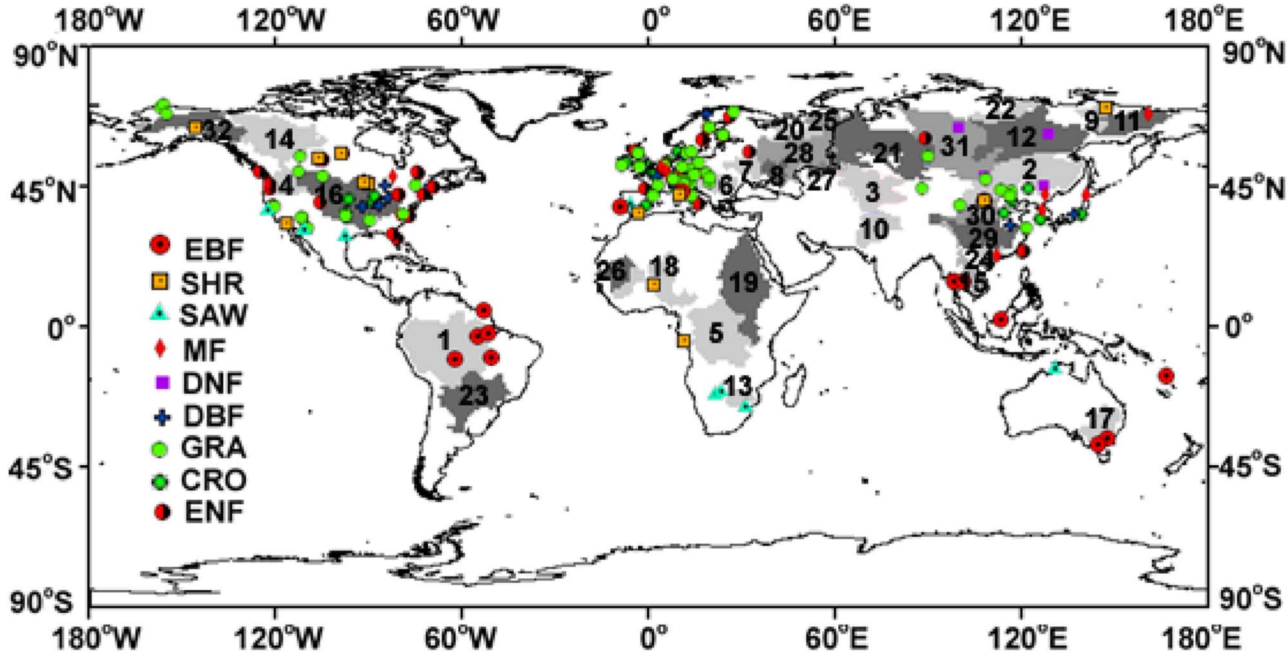

Fig. 1. Map of the 200 eddy covariance flux tower sites and the 32 large basins used in this study. 32 large basins are shown: 1. Amazon, 2. Amur, 3. Aral, 4. Columbia, 5. Congo, 6. Danube, 7. Dnieper, 8. Don, 9. Indigirka, 10. Indus, 11. Kolyma, 12. Lena, 13. Limpopo, 14. Mackenzie, 15. Mekong, 16. Mississippi, 17. Murray-Darling, 18. Niger, 19. Nile, 20. Northern Dvina, 21. Ob, 22. Olenek, 23. Parana, 24. Pearl, 25. Pechora, 26. Senegal, 27. Ural, 28. Volga, 29. Yangtze, 30. Yellow, 31. Yenisei, 32. Yukon. Nine major biomes are shown: DBF: deciduous broadleaf forest; DNF: deciduous needleleaf forest; EBF: evergreen broadleaf forest; ENF: evergreen needleleaf forest; MF: mixed forest; SAW: savannas and woody savannas; SHR: open shrubland and closed shrubland; CRO: cropland; GRA: grassland, urban and built-up, barren or sparsely vegetated.

were indicated as missing. Similarly, the monthly data were aggregated from the daily data (Jia et al., 2012; Liu et al., 2011; Liu et al., 2013; Xu et al., 2013). Considering that the *EC* method suffers an energy imbalance problem, the measured *ET* was corrected based on the method proposed by Twine et al. (2000).

$$ET_{cor} = (R_n - G)/(H_{ori} + ET_{ori}) \times ET_{ori} \quad (2)$$

where ET_{cor} is the corrected *ET*, and H_{ori} and ET_{ori} are the uncorrected *H* and *ET*, respectively.

2.1.2. Satellite and reanalysis data

To examine the performances of all *ET* algorithms for all flux tower sites, the daily R_n, R_s, T_a, $T_{\max}$, *e*, *RH*, and *WS* products with a spatial resolution of $1/2° \times 2/3°$ from *MERRA* data provided by the National Aeronautics and Space Administration (*NASA*) were used in this study. Details of the *MERRA* dataset are available from *NASA* website (http://gmao.gsfc.nasa.gov/research/merra). We interpolated the daily *MERRA* data spatially to 1 km based on the bilinear method. Accordingly, the 8-day *MODIS FPAR/LAI* (*MOD15A2*) product (Myneni et al., 2002) and the 16 day *MODIS NDVI* (*MOD13A2*) product (Huete et al., 2002) at 1-km spatial resolution were used to drive all *ET* algorithms. The daily *FPAR/LAI* (*NDVI*) values were temporally interpolated from the 8-day (16-day) averages using linear interpolation. When the data were missing, we temporally filled the missing *FPAR*, *LAI* and *NDVI* with 1-km *MODIS* pixel based on the method described by Zhao et al. (2005), which exploits the closest reliable 16 day (8 day) values to replace the missing data.

To generate the global terrestrial *ET* product at a spatial resolution of 0.05° from 2003 to 2005, we interpolated the daily *MERRA* data spatially to 0.05° based on the bilinear method. We also used the Collection 5 *MODIS NDVI* (*MOD13C1*: *CMG*, 0.05°), Collection 4 *MODIS* land cover (*MOD12C1*: *CMG*, 0.05°) (Friedl et al., 2002) and the Collection 5 *MODIS FPAR/LAI* (*MOD15A2*, 1-km) to drive the three satellite-based *ET* algorithms. The 1-km *LAI/FPAR* was also aggregated into 0.05° gridded data using the bilinear method.

2.1.3. Data at global large basins

A total of 32 global large basins covering areas from 2.3×10^5 to $6.0 \times 10^5\,km^2$ were collected from Pan et al. (2012) (Fig. 1). Basin averaged monthly data, including precipitation (*P*) and streamflow (*Q*), were used and aggregated into annual data (2003–2005). The *P* and *Q* gridded products at a spatial resolution of 0.5° were generated based on a constrained Kalman filter technique that merged a number of global datasets including in situ observations, remote sensing retrievals, land surface model simulations and global reanalysis (Pan et al., 2012). In addition, the Gravity Recovery and Climate Experiment (*GRACE*) satellites datasets (Center for Space Research Release 4: *CSR RL04*) from 2003 to 2005 were also interpolated into 0.5° and used to obtain the water storage changes (*TWSC*) (Swenson and Wahr, 2002). At the basin scale, these gridded variables (*P*, *Q* and *TWSC*) products were all averaged to derive *ET* for the global *ET* algorithms assessment.

2.2. Three process-based ET algorithms

Three process-based *ET* algorithms were used in this study, and the algorithms are illustrated using their abbreviations in the figure legends, for example, the *MODIS ET* product algorithm is abbreviated as *MOD16*. Table 1 describes the three process-based algorithms in detail.

2.2.1. MODIS ET product algorithm

The *MODIS ET* product algorithm (*MOD16*) is an improved Penman-Monteith equation (Mu et al., 2011), which is based on a beta version (Mu et al., 2007) after being adapted by Cleugh et al. (2007):

$$ET = \frac{\Delta R_n + \rho C_p (e_s - e)/r_a}{\Delta + \gamma (1 + r_s/r_a)} \quad (3)$$

where e_s is saturated water vapor pressure, Δ is the slope of the curve relating saturated water vapor pressure to temperature, ρ is the air density, C_p is the specific heat capacity of air, γ is the psychrometric constant, r_a is the aerodynamic resistance, and r_s is the surface resistance. The *MOD16 ET* algorithm is the modified beta version (Mu

Table 1
Summary of the six *ET* models and forcing variables. *ET* is the total evapotranspiration; ET_c is the canopy transpiration; ET_s is the soil evaporation; ET_i is the interception evaporation; *ET1* is the total evapotranspiration derived from the *MOD16* algorithm; *ET2* is the total evapotranspiration derived from the *PT-JPL* algorithm; and *ET3* is the total evapotranspiration derived from the *SEMI-PM* algorithm.

ID	ET algorithm	Forcing Inputs	Outs	References
1	*MODIS ET* products algorithm (*MOD16*)	R_n, T_a, T_{min}, *RH*, *FPAR*, *LAI*, *PFTs*	*ET1*, ET_c, ET_s, ET_i	Mu et al. (2011)
2	Priestley-Taylor *ET* algorithm of Jet Propulsion Laboratory (*PT-JPL*)	R_n, T_a, T_{max}, *RH*,*FPAR*, *LAI*, *NDVI*	*ET2*, ET_c, ET_s, ET_i	Fisher et al. (2008)
3	Semi-empirical Penman ET algorithm (*SEMI-PM*)	R_s, T_a, *RH*,*WS*, *NDVI*	*ET3*	Wang et al. (2010a)
4	Bayesian model averaging method (*BMA*)	*ET1*,*ET2*,*ET3*	*ET*	Raftery et al. (2005)
5	General regression neural networks (*GRNNs*)	*ET1*,*ET2*,*ET3*	*ET*	Specht (1991)
6	Support vector machine (*SVM*)	*ET1*,*ET2*,*ET3*	*ET*	Vapnik (1995)

et al., 2007) by calculating *ET* as the sum of daytime and nighttime components; modifying vegetation cover fraction with *FPAR* derived from *MOD15A2* product; modifying calculations of aerodynamic, boundary-layer, and canopy resistance and dividing the canopy and soil into wet and dry components, respectively (Mu et al., 2011). The total *ET* is the sum of interception evaporation (ET_i), canopy transpiration (ET_c), saturated wet soil evaporation (ET_{sw}) and unsaturated soil evaporation (ET_{su}).

$$ET = ET_i + ET_c + ET_{sw} + ET_{su} \tag{4}$$

$$ET_i = \frac{[\Delta R_{nc} + \rho C_p(e_s - e)f_c/rhrc]f_{wet}}{\Delta + \frac{P_a \times C_p \times rvc}{\lambda \times \varepsilon \times rhrc}} \tag{5}$$

$$ET_c = \frac{[\Delta R_{nc} + \rho C_p(e_s - e)f_c/r_a](1 - f_{wet})}{\Delta + \gamma(1 + r_s/r_a)} \tag{6}$$

$$ET_{sw} = \frac{[\Delta R_{ns} + \rho C_p(e_s - e)(1 - f_c)/r_{as}]f_{wet}}{\Delta + \gamma \times r_{tot}/r_{as}} \tag{7}$$

$$ET_{su} = \frac{[\Delta R_{ns} + \rho C_p(e_s - e)(1 - f_c)/r_{as}](1 - f_{wet})}{\Delta + \gamma \times r_{tot}/r_{as}} \times \left(\frac{RH}{100}\right)^{VPD/\beta} \tag{8}$$

where R_{nc} is the net radiation to the canopy, R_{ns} is the net radiation to the soil, f_c is the vegetation cover fraction, f_{wet} is the relative surface wetness cover from the *PT-JPL* model (Fisher et al., 2008), *VPD* is the vapor pressure deficit, β is a constant (200), *rhrc*is the aerodynamic resistance on the wet canopy surface, *rvc*is the wet canopy resistance, r_{tot} is the total aerodynamic resistance to vapor transport, and r_{as} is the aerodynamic resistance at the soil surface. Further details of the *MOD16* algorithm can be found in Mu et al. (2011).

2.2.2. Priestley-Taylor-Based ET algorithm

Starting with the Priestley and Taylor (1972) equation for potential *ET*, Fisher et al. (2008) developed the *PT-JPL* model by introducing both ecophysiological (*FPAR* and *LAI*) and atmospheric (*RH* and *VPD*) constraints without using any ground-based observed data to reduce potential *ET* to actual *ET*. The total *ET* is partitioned into three components, the soil evaporation (ET_s), the canopy transpiration (ET_c) and the interception evaporation (ET_i).

$$ET = ET_s + ET_i + ET_c \tag{9}$$

$$ET_s = \alpha\frac{\Delta}{\Delta + \gamma}[f_{wet} + f_{sm}(1 - f_{wet})](R_{ns} - G) \tag{10}$$

$$ET_c = \alpha\frac{\Delta}{\Delta + \gamma}f_g f_T f_m(1 - f_{wet})R_{nc} \tag{11}$$

$$ET_i = \alpha\frac{\Delta}{\Delta + \gamma}f_{wet}R_{nc} \tag{12}$$

$$f_g = \frac{F_{APAR}}{F_{IPAR}} \tag{13}$$

where α is the Priestley-Taylor (*PT*) coefficient for a wet surface condition (1.26), f_{sm} is the soil moisture constraint, f_T is the plant temperature constraint, f_g is the green canopy fraction, f_m is the plant moisture constraint, F_{APAR} is the fraction of *PAR* absorbed by green vegetation cover and F_{IPAR} is the fraction of *PAR* intercepted by total vegetation cover, which is estimated with *NDVI* (Fisher et al., 2008). Details of the *PT-JPL* algorithm were fully described by Fisher et al. (2008).

2.2.3. Semi-empirical Penman algorithm

Based on the Penman (1948) equation, the Semi-empirical Penman *ET* algorithm (*SEMI-PM*) was developed by Wang et al. (2010a). This algorithm considers that the total *ET* is composed of two components, the energy control component (ET_e) and the aerodynamic control component (ET_a).

$$ET = a_1(ET_e + ET_a) + a_2(ET_e + ET_a)^2 \tag{14}$$

$$ET_e = \frac{\Delta}{\Delta + \gamma}R_s[a_3 + a_4 NDVI + (1 - \frac{RH}{100})(a_5 + a_6 NDVI)] \tag{15}$$

$$ET_a = \frac{\gamma}{\Delta + \gamma}WS[a_7 + (1 - \frac{RH}{100})(a_8 + a_9 NDVI)]VPD \tag{16}$$

The empirical coefficients were derived from observed data collected at 64 globally distributed flux tower sites. The algorithm considers different climate conditions and is simple to operate. The algorithm includes *WS*, which may play an important role in annual or decadal *ET* variability (McVicar et al., 2012; Wang et al., 2010a,b).

2.3. Support vector machine

The support vector machine (*SVM*) method was used in this study to merge the three satellite-based *ET* algorithms to estimate the global terrestrial *ET*. For *SVM*, linear models in the new feature can be used to resolve the original nonlinear problem because a multi-dimensional input space is more likely to be linearly separable in a new feature space (Vapnik, 1995; Yang, 2006; Nurmemet et al., 2015). For a given training dataset$\{(x_i, y_i), 1 \le i \le n\}$, x_i is the input of the *ET* derived from each single *ET* algorithm, y_i is the target concept of the ground-measured *ET*, and *n* is the number of training examples. To obtain a functional dependency *f*(*x*) between the inputs *x* and the target *y* derived from the set of independent and identically distributed observations, the objective function for the *SVM* method (Vapnik, 1995) can be formulated as follows:

$$f(x) = < w, x_i > + b \tag{17}$$

$$\text{Minimize } \frac{1}{2}\left|\left|w\right|\right|^2 + K\sum_{i=1}^{n}(\eta_i + \eta_i^*) \tag{18}$$

$$\text{Subject to } < w, x_i > + b - y_i \le \varepsilon + \eta_i^* \tag{19}$$

$$y_i - < w, x_i > - b \le \varepsilon + \eta_i \tag{20}$$

$\eta_i, \eta_i^* \ge 0$, $i = 1,\ldots, n$ (21)

where *x* is the input vector, *w* is the weights vector norm, $< w, x_i >$ is the dot product of *x* and *w*,*b* is a bias,*K* is a cost of errors, ε is Vapnik's insensitive loss function, and η_i denotes the predicted value to

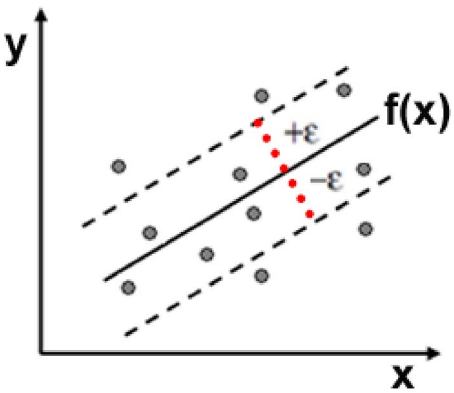

Fig. 2. One-dimensional linear regression with ε-insensitive band for the *SVM* method.

be above the true value by more than ε, and $\eta_i^*$to be below the true value by more than ε. Fig. 2 illustrates the one-dimensional linear regression function with an ε-insensitive band. Data points out of the ε-insensitive band are called support vectors, and only support vectors contribute to the optimization solution (Yang, 2006; Shrestha and Shukla, 2015).

The optimization problem presented in Eqs. (18)–(21) can be solved based on the technique of Lagrange multipliers (a and a^*) by the following equation:

$$\text{Maximize } < a, a^* > = \sum_{i=1}^{n} y_i(a_i - a_i^*) - \varepsilon \sum_{i=1}^{n} (a_i + a_i^*) - \frac{1}{2} \sum_{i=1}^{n}\sum_{j=1}^{n} (a_i - a_i^*)(a_j - a_j^*) < x_i, x_j> \quad (22)$$

$$\text{Subject to } \sum_{i=1}^{n} (a_i^* - a_i) = 0,\ a_i, a_i^* \in [0, K] \quad (23)$$

Then, the approximating $f(x)$ function can be written as:

$$f(x) = \sum_{i=1}^{n} (a_i^* - a_i) < x, x_i > + b \quad (24)$$

The kernel function $u(x, x_i)$ is introduced to bring the training data into a high dimension feature space and Eq. (24) can be updated as:

$$f(x) = \sum_{i=1}^{n} (a_i^* - a_i) u(x, x_i) + b \quad (25)$$

We used the Radial basis function (*RBF*) kernel in this study because previous studies have shown that the *RBF* kernel performs better than other kernels (Dibike et al., 2001; Khalil et al., 2006). The *RBF* kernel function can be expressed as:

$$u(x, x_i) = \exp(-\frac{1}{2\sigma_2}\left|\left|x - x_i\right|\right|^2) \quad (26)$$

where σ is a variance. Further details of the *SVM* method can be found in Vapnik (1995).

2.4. Other multi-model ensemble methods

2.4.1. Bayesian model averaging method

The Bayesian model averaging (*BMA*) method is an approach to combine the forecast densities predicted by different models, producing a new forecast probability density function (*PDF*) (Duan and Phillips, 2010; Raftery et al., 1995; Yao et al., 2016). According to the *BMA* method, the combined forecast *PDF* of a variable y (*ET* in this study), given the independent predictions of k models, [A_1, A_2, …, A_k], and the corresponding *EC ET* observation, O, can be expressed as:

$$p(y\left|A_1, A_2, \ldots, A_k, O) = \sum_{i=1}^{k} p(A_i|O)p(y\right|A_i, O) \quad (27)$$

Where $p(A_i|O)$ is the posterior distribution of y for A_i. $p(y|A_i, O)$ is the predictive model likelihood being correct using the observations, O, and it can be considered as the weight (C_i) of model A_i. Thus, Eq. (25) can be written as:

$$p(y\left|A_1, A_2, \ldots, A_k, O) = \sum_{i=1}^{k} C_i p(y\right|A_i, O) \quad (28)$$

C_i can be calculated using the maximum likelihood function, which has been acquired from the expectation maximization (*EM*) algorithm (Raftery et al., 2005). Further details of the *EM* algorithm and the *BMA* method can be found in Duan and Phillips (2010).

2.4.2. General regression neural networks

General regression neural networks (*GRNNs*) are the generalizations of radial basis function networks and probabilistic neural networks (Specht, 1991). The functional estimate of the *GRNNs* method is calculated directly from the training data without iterative training. The basic structure of the *GRNNs* method includes four layers: the input layer, the pattern layer, the summation layer and the output layer (Jia et al., 2015; Xiao et al., 2014). The input layer includes the input variables (*ET* estimated from each single algorithm) and the output layer provides the *GRNNs* method estimated *ET* by merging the three algorithms. The kernel function of the *GRNNs* method meets the Gaussian distribution and the fundamental formulation can be written as:

$$Y'(X) = \frac{\sum_{i=1}^{n} Y_i \exp(-\frac{D_i^2}{2\sigma^2})}{\sum_{i=1}^{n} \exp(-\frac{D_i^2}{2\sigma^2})} \quad (29)$$

$$D_i^2 = (X - X_i)^T(X - X_i) \quad (30)$$

where $Y'(X)$ is the estimation corresponding to the input vectors X, Y_i is the output vector corresponding to the ith training input vector X_i, n is the number of samples, D_i^2 is the squared Euclidean distance between X and X_i, and σ refers to a smoothing parameter that controls the size of the receptive region. σ affects the weights and accuracy of the *GRNNs* method for *ET* prediction. The holdout method was used to determine σ by removing one sample from the training data and then constructing the *GRNNs* using all of the remaining training samples. The training processes were terminated once the minimum of the cost function of σ was reached:

$$f(\sigma) = \frac{1}{n}\sum_{i=1}^{n} (\overline{\overline{Y_i}}(X_i) - Y_i)^2 \quad (31)$$

where $\overline{\overline{Y_i}}(X_i)$ is the estimate corresponding to X_i based on the *GRNNs* trained over all of the training samples, except the ith sample. More details of the *GRNNs* method can be found in Specht (1991).

2.5. Evaluation methods

2.5.1. SVM experimental setup based on cross-validation

To merge three satellite-based *ET* algorithms, we trained the *SVM* method based on the ground-measured *ET* for period of 2000–2009 and the corresponding estimated *ET* using the individual algorithms. To remove the influence of the input variables with different absolute magnitudes, we scaled all of the input variables on the range of −1 to 1.

We trained and tested the models as follows. Firstly, we selected the radial basis function (*RBF*) kernel because it determines the performance of machine learning methods and requires only one parameter (σ). Secondly, we initially set a coarse grid search for $K(2^{-1},2^0,\ldots,2^4)$, ε $(2^{-5},2^{-4},\ldots,2^{-2})$ and σ $(2^{-3},2^{-2},\ldots,2^4)$, and further found the K, ε and σ with the lowest mean cross-validation root mean squared error (*RMSE*). Based on the selected K, ε and σ, a final training of the *SVM*

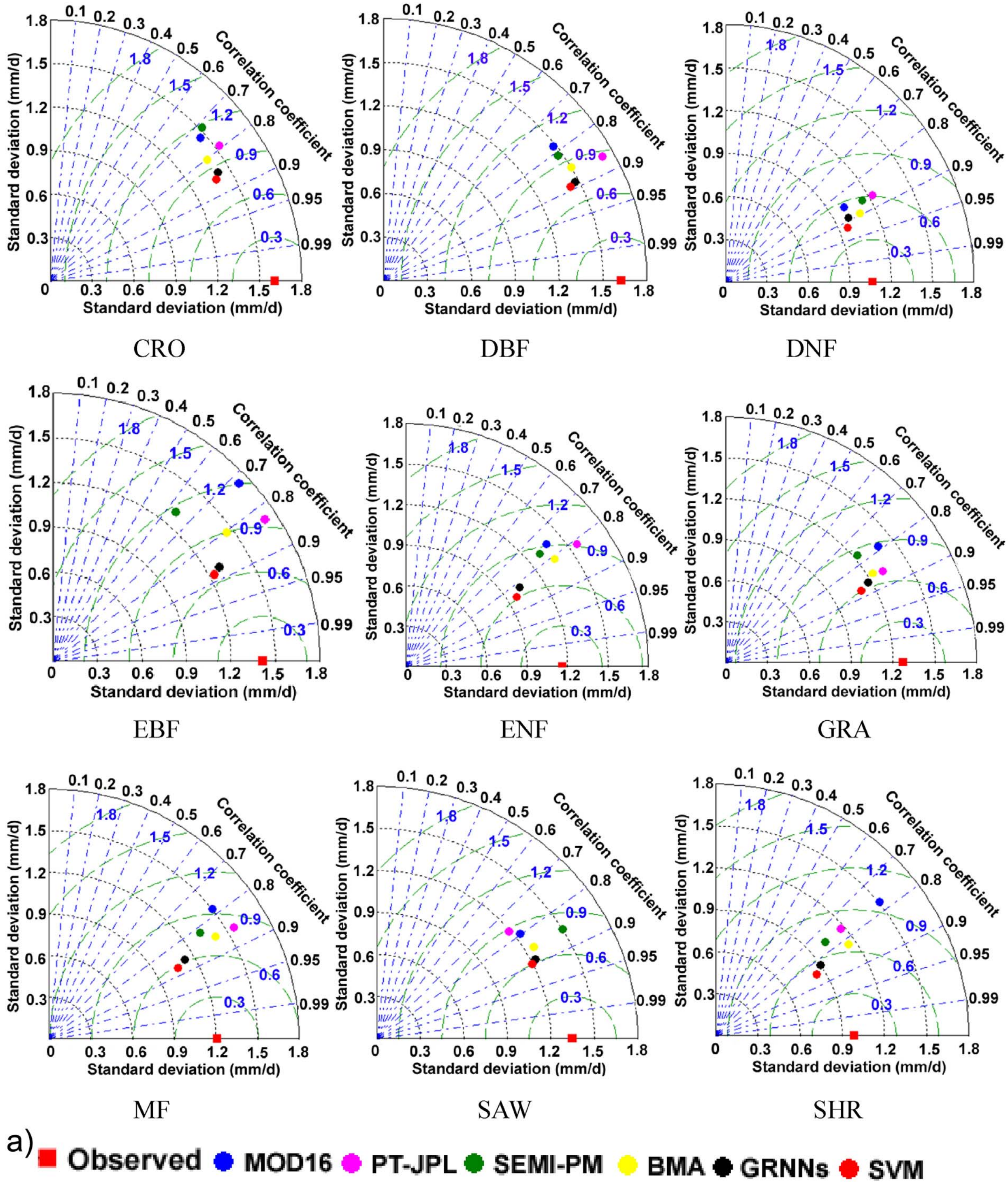

Fig. 3. a) Taaylor diagrams for the daily *ET* observations and *ET* estimates using the different algorithms driven by tower-specific meteorology at the 200 *EC* sites. The dotted circular lines connecting the *X* and *Y* axes represent the *STD*, the dotted radial lines are the correlation (*R*), and the green curves denote the *RMSE* with respect to the reference dataset. The simulated *ET* based on the *SVM* method, the *GRNNs* method and the *BMA* method and by merging three satellite-based *ET* algorithms for each of the four groups was independently validated using the samples of the remaining three groups (mm/d refers to mm per day). b) Same as Fig. 3a) but for the results driven by *MERRA* meteorology at the 200 *EC* sites. (For interpretation of the references to colour in this figure legend, the reader is referred to the web version of this article.)

for 2000–2009 *EC* data was performed. Thirdly, we trained and tested the performances of the *SVM* method using a fourfold cross-validation method. The training data sets were stratified into four folds, each containing ca. 25% of the data (Jung et al., 2011). Entire sites were assigned to each fold (Jung et al., 2011; Tramontana et al., 2016). *SVM* training is performed four times on three of the groups, with the remaining group reserved for testing and parameters with the lowest cross-validation errors are chosen. Moreover, we evaluated the performance of the *SVM* method by comparing the *SVM* results with the *BMA* method, the *GRNNs* method and the *WB* equation. Here, similar procedures were performed to design the *GRNNs* experimental setup. Finally, we trained the *SVM* method using all available data to merge the three satellite-based *ET* algorithms to generate global terrestrial *ET* product.

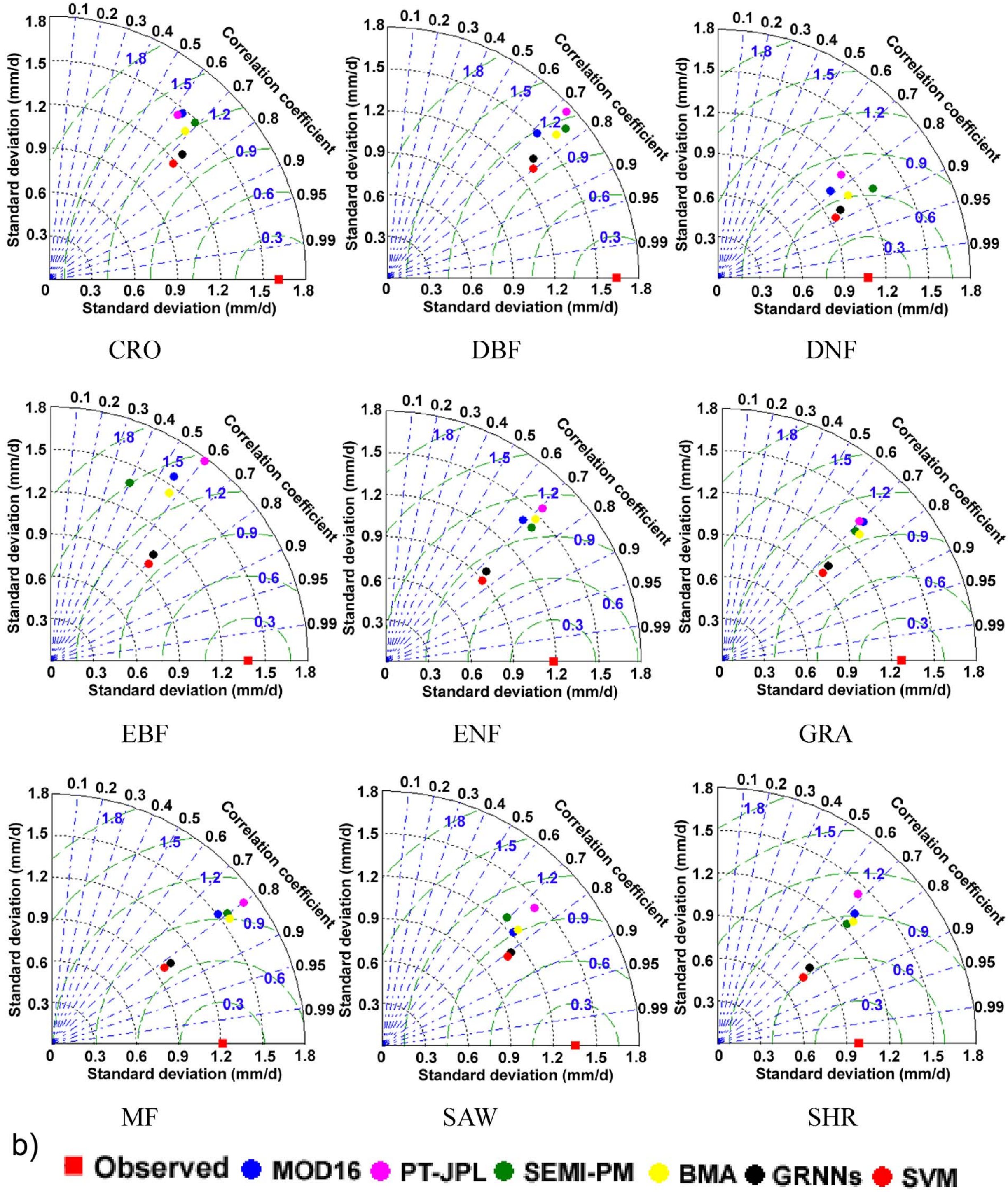

Fig. 3. (*continued*)

2.5.2. Taylor diagrams

Taylor diagrams were used to assess the performance of the *SVM* method, the *GRNNs* method, the *BMA* method and the individual *ET* algorithms (Taylor, 2001). A Taylor diagram is a polar-style graph that includes the standard deviation (*STD*) between the simulations and the observations, the correlation coefficient (*R*) and the centered *RMSE*. In a Taylor diagram, *STD* is the radial distance from the origin, *R* is characterized by the cosine of the azimuth angle, and *RMSE* refers to the radial distance from the observed point. In addition, the average bias and *p* values for the estimated *ET* and ground-measured *ET* were used to assess the simulation errors in the different *ET* algorithms.

2.5.3. The Akaike information criterion and the Bayesian information criterion

The Akaike information criterion (*AIC*) and the Bayesian information criterion (*BIC*) were also used to evaluate the performance of the *SVM* method, the *GRNNs* method, the *BMA* method and the individual *ET* algorithms. The *AIC* is a measure of the quality of each model, relative to each of the other models for a given set of data (Akaike, 1974; Loehlin, 1992) and the *AIC* value of the model can be expressed as:

$$AIC = -2\ln L + 2c \tag{32}$$

Where *L* is the maximum value of the likelihood function for the model and *c* is the number of free parameters in the model. The model with the smallest *AIC* is the best performance. The *BIC* is also an indicator for assessing model performance, but it takes into account the number of data points, *n* (Schwarz, 1978). The *BIC* is formally defined as:

$$BIC = -2\ln L + c\ln(n) \tag{33}$$

The model with lowest *BIC* values is preferred. Thus, the good performance of different algorithms in this study is normally based on the low *AIC* and *BIC* values.

2.5.4. Water balance equation

The *SVM*-merged *ET* estimation over the basin and regional scale was evaluated based on the water balance equation. *ET* can be calculated based on the precipitation (*P*), the streamflow (*Q*) and the water storage changes (*TWSC*) within a water-closed basin.

$$ET = P - Q - TWSC \tag{34}$$

Of the four water budget components, *P* and *Q* can be acquired from the multiple datasets that were produced by Pan et al. (2012), and *TWSC* can be acquired from the *GRACE* data. Thus, terrestrial *ET* can be inferred using Eq. (34) within the 32 global large basins.

2.5.5. Contribution of each individual algorithm on merged ET

To test the contribution of each individual algorithm on *SVM*-merged *ET*, we removed one of the individual algorithms and replicated the cross-validation training process. The mean cross-validation *RMSE* and the squared correlation coefficient (R^2) from the cross-validation training process were quantitatively used to evaluate the contribution of each individual algorithm.

3. Results

3.1. The performance of the SVM method at the site scale

Fig. 3a) and b) show the Taylor diagrams for the daily *ET* observations and *ET* estimates using the different algorithms driven by tower-specific (defined as “ground-measured”) meteorology and *MERRA* meteorology at the 200 *EC* sites, respectively. Figs. 3 and 4 showed that the six algorithms exhibited substantial differences for each *PFT*. For the *MF*, *DNF* and *DBF* sites, the *SVM* method driven by tower-specific (*MERRA*) meteorology behaved better than the *MOD16* algorithm, the *PT-JPL* algorithm, the *SMEI-PM* algorithm, the *BMA* method and the *GRNNs* method, with an R^2 of greater 0.78 (0.68), ($p < 0.01$), a low bias ranging from −0.01 to 0.01 (−0.02–0.02) mm/day and smaller *RMSEs* of less than 0.70 (0.80) mm/day. Similarly, for the *ENF* and *EBF* sites using the *SVM* method driven by tower-specific (*MERRA*) meteorology, the *RMSE* of the estimated *ET* versus ground observations was approximately 0.66 (0.93) mm/day and the R^2 is approximately less than 0.75 (0.61) ($p < 0.01$), but it still presented better performance than the *BMA* method, the *GRNNs* method and the individual algorithms. For all of the crop sites, the estimated *ET* using the *SVM* method for tower-specific (*MERRA*) meteorology inputs still exhibited the lowest *RMSE* of 0.81 (1.08) mm/day, and the highest R^2 of 0.74 (0.56) at the 99% level of confidence, compared with the *BMA* method, the *GRNNs* method and the individual algorithms. Almost all three individual algorithms showed the poor performance at the crop sites and so did the three merged estimates. Therefore, a poor model performance of the *SVM* method was also found at these crop sites. For the other *PFTs* (*GRA*, *SAW* and *SHR*) sites, the average *RMSE* was much lower and the average R^2 was slightly higher for the *SVM* method compared with the other five algorithms. As another machine learning method, the *GRNNs* method was superior to the *BMA* method and the individual algorithms for all *PFTs*, but it still had lower performance with lower R^2 and higher *RMSE* than the *SVM* method. For all of the *PFTs*, the *SVM* method was superior to the *GRNNs* and the *BMA* methods. Overall, compared with the individual algorithms, the *RMSE* of the *SVM* method driven by tower-specific (*MERRA*) meteorology decreased the *RMSE* by approximately 0.20 (0.15) mm/day for most forest sites and approximately 0.30 (0.20) mm/day for most crop and grass sites and increased the R^2 by more than 0.10 (0.08) (95% confidence) for most flux tower sites.

Fig. 5 demonstrated the *AIC* and *BIC* values calculated from six algorithms. It is clear that the *SVM* method driven by tower-specific (*MERRA*) meteorology gave the lowest *AIC* and *BIC* values for different *PFTs* when compared to those obtained from other five models. However, the *AIC* and *BIC* values of the *SVM* method are slightly lower than those of the *GRNNs* method. The *GRNNs* method provided the second best accuracies. Therefore, the *SVM* method provides a better representation of the *ET* data of the globally distributed eddy covariance tower sites used in this study than other five models.

Fig. 6 shows the *SVM* exhibited most features of measured *ET* seasonality in the ground-measured test data for different *PFTs*. In comparison to the *BMA* method, the *GRNNs* method and the individual algorithms, the *SVM* method produced seasonal *ET* variations that were closest to the ground-measured *ET*. The bias of the estimated *ET* based on the *SVM* method varies from −0.04 to 0.03 mm/day, the R^2 varies from 0.73 to 0.83, and the *RMSE* varies from 0.41 to 0.80 mm/day. Fig. 7 shows the frequency distributions of the predictive errors in all six algorithms driven by tower-specific and *MERRA* meteorology, respectively. The errors distributions of the *SVM*-merged *ET* estimates are more closely centered on zero and the *SVM* method decreased the substantial positive and negative biases. Therefore, the *SVM* strategy can capture the *ET* variance and has good model performance.

To improve global terrestrial *ET* estimation using the *SVM* method, all of the data collected at the 200 flux tower sites were used as training data to determine the nonlinear combinations of the three satellite-based algorithms. Figs. 8 and 9 present the scatter plots between the monthly observed *ET* at all of the 200 flux tower sites and the *ET* estimates for the six algorithms driven by tower-specific and *MERRA* meteorology, respectively. The results show that the *SVM* method has the best performance, with the highest R^2 (0.90 and 0.80) ($p < 0.01$) and the lowest *RMSE* (11.15 mm/month and 14.71 mm/month) compared with the other five algorithms. Previous substantial studies also illustrated that the *SVM* method, trained with hydro-climatic inputs, yields better *ET* estimates than do neural networks and other methods in a series of cross-validation experiments (Yang, 2006; Shrestha and Shukla, 2015). Therefore, the improved accuracy of the *SVM* method by merging the three satellite-based algorithms makes it useful for estimating the regional terrestrial *ET*.

3.2. Evaluation of the SVM-merged ET at the basin level

We compared the estimated global *ET* using six algorithms driven by *MERRA* meteorology with the inferred *ET* from basin-scale water balance calculations for 32 major global basins (Fig. 10). In comparison to the *BMA* method, the *GRNNs* method and the individual algorithms, the *SVM* method still had the best performance with the lowest *RMSE* of 90.38 mm and the highest R^2 of 0.89 ($p < 0.01$) over the 32 watersheds. Large differences between the *SVM*-merged *ET* and the inferred *ET* occurred in some of the high latitude basins, such as the Pechora, Yukon and Ural basins. The mean difference in those basins was approximately 110 mm/year. This discrepancy may be partially attributable to the few *ET* observations, which reduced the accuracy of the *SVM*-merged *ET*. Pan et al. (2012) showed that the global terrestrial water budget (*P* and *Q*) determined by merging a number of global datasets has a higher accuracy compared with that based on the individual datasets, but there are still small biases in some regions. Therefore, the biases of *P*, *Q* and *TWSC* from different data sets can also result in errors in the inferred *ET*, which will contribute to *SVM*-merged *ET* and inferred *ET* differences in those regions. Although there were large differences between the *SVM*-merged and inferred *ET* in some of the basins, the good agreement based on a verification of the water

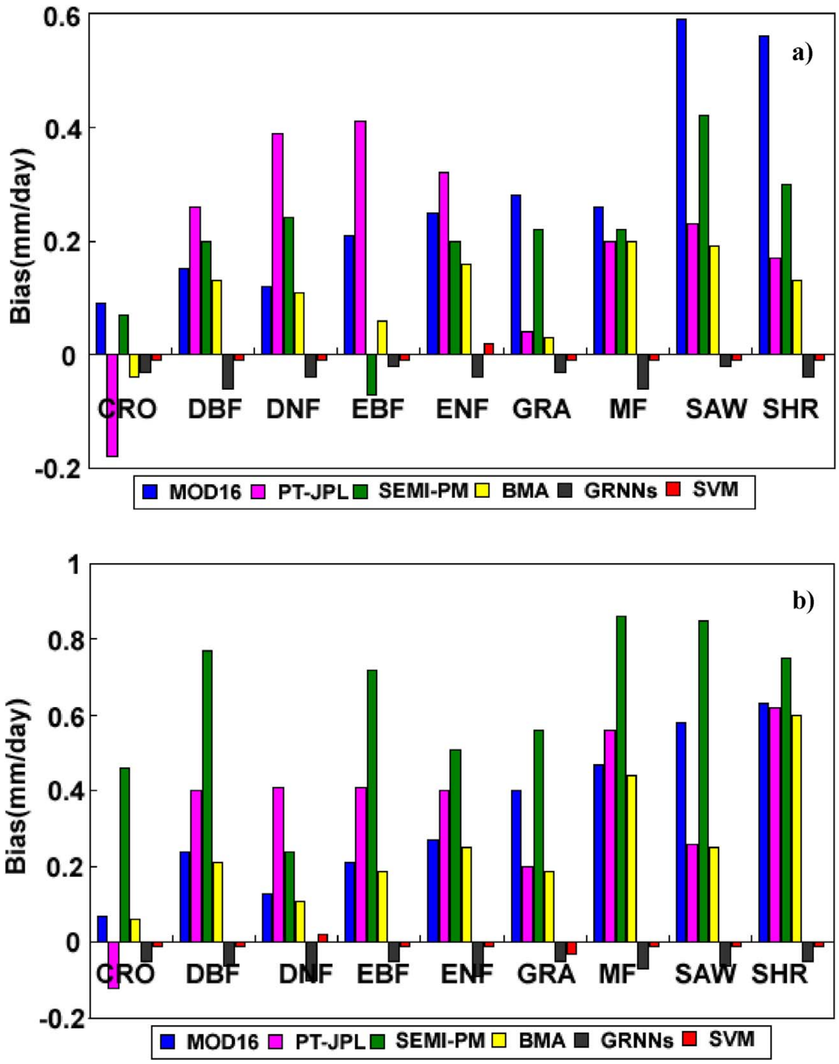

Fig. 4. The averaged biases of estimated *ET* using six models driven by a) tower-specific and b) *MERRA* meteorology versus ground-measured *ET* for nine *PFTs* at the 200 flux tower sites.

balance approach for most of the basins demonstrates that the *SVM* method was reliable.

3.3. Contribution of each individual algorithm on SVM-based ET variations

Removing the *SEMI-PM* algorithm driven by tower-specific meteorology reduced the largest performance of *SVM* in cross-validation error analysis for *DNF*, *ENF* and *MF PFTs* (Fig. 11). R^2 decreased by approximately 0.10 and *RMSEs* increased by approximately 0.08 mm/day. Removal of the *MOD16* algorithm caused the secondary performance reduction for all above three *PFTs*, leading to decreased R^2 of approximately 0.05 and increased *RMSEs* of 0.06 mm/day. Removing the *PT-JPL* algorithm yielded comparatively minor changes with the R^2 reduced by about 0.02 and *RMSEs* rose by 0.02 mm/day. In contrast, the largest performance reduction for other *PFTs* was to remove the *PT-JPL* algorithm: the *RMSEs* increased by more than 0.09 mm/day and the R^2 reduced by 0.12. While removal of the *MOD16* algorithm resulted in small performance reduction for other *PFTs*. Therefore, the *SEMI-PM* algorithm captured most of the *ET* variations for *DNF*, *ENF* and *MF PFTs*, while the *PT-JPL* algorithm has the highest contribution to *SVM*-merged *ET* for other *PFTs*. Although our input each individual algorithm ranking was based on the tower-specific meteorology, similar conclusions can be drawn when using the *MERRA* meteorology as inputs.

3.4. SVM-merged global terrestrial ET patterns

We applied the *SVM* method, the *GRNNs* method, the *BMA* method and the individual algorithms with the *MERRA* meteorology and *MODIS* product to estimate annual *ET* globally at a 0.05° spatial resolution from 2003 to 2005. Over the 2003–2005 study period, average annual *ET* from the *SVM* method has the smallest values of 85 mm/yr in cold and arid regions, intermediate values of 321 mm/yr in the temperate regions, and highest values of 1279 mm/yr over the tropical and subtropical forests of the Congo basin in central Africa, the Amazon basins in South America and the Indonesia rain forests in Southeast Asia (Fig. 12). Compared with the *MOD16* algorithm, the *PT-JPL* algorithm and the *BMA* method, the *SVM* method yields lower annual global terrestrial *ET* in rain forests regions (Indonesia, Amazon and Congo) and higher *ET* in arid and semi-arid regions (Fig. 13). However, there are opposite spatial differences between the *SVM* method and the other two methods (*GRNNs* and *SEMI-PM*).

The global terrestrial average annual *ET* based on the *SVM* method was 471.7 mm/yr, which was lower than the *ET* values that were based on *PT-JPL* (508.8 mm/yr), *SEMI-PM* (517.2 mm/yr), *BMA* (486.1 mm/yr) and *GRNNs* (475.9 mm/yr), and higher than the *ET* values that were based on *MOD16* (433.7 mm/yr). The average annual *ET* for *CRO*, *GRA*, *SAW*, *DNF*, *ENF*, *DBF* and *MF* was 485 mm/yr, 322 mm/yr, 616 mm/yr, 244 mm/yr, 185 mm/yr, 589 mm/yr and 381 mm/yr, respectively. The seasonal patterns of *ET* averaged from 2003 through 2005 based on the

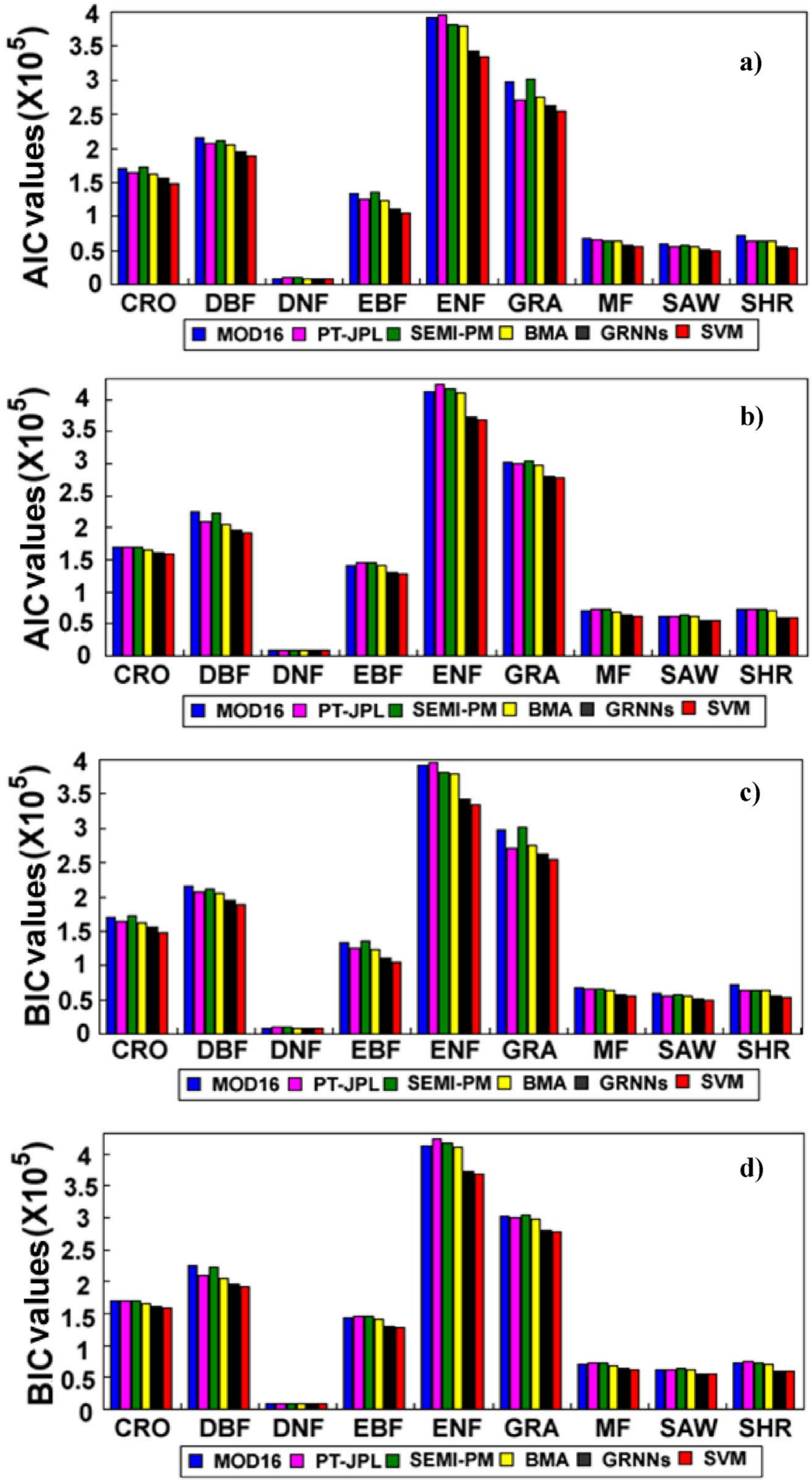

Fig. 5. The *AIC* and *BIC* values of six models. The *AIC* values of estimated *ET* using six models driven by a) tower-specific and b) *MERRA* meteorology for nine *PFTs* at the 200 flux tower sites. The *BIC* values of estimated *ET* using six models driven by c) tower-specific and d) *MERRA* meteorology for nine *PFTs* at the 200 flux tower sites.

SVM method driven by the *MERRA* meteorology and *MODIS* product illustrated obviously seasonality for most *PFTs* (Fig. 14). However, there is no seasonality for *EBF* and *SAW* with high *ET* values around the whole year.

4. Discussion

4.1. The performance of the SVM method

By merging three process-based *ET* algorithms, the *SVM* method not only preserved the partial dynamic information of *ET* process, but yielded the global terrestrial *ET* with high accuracy. We found that the

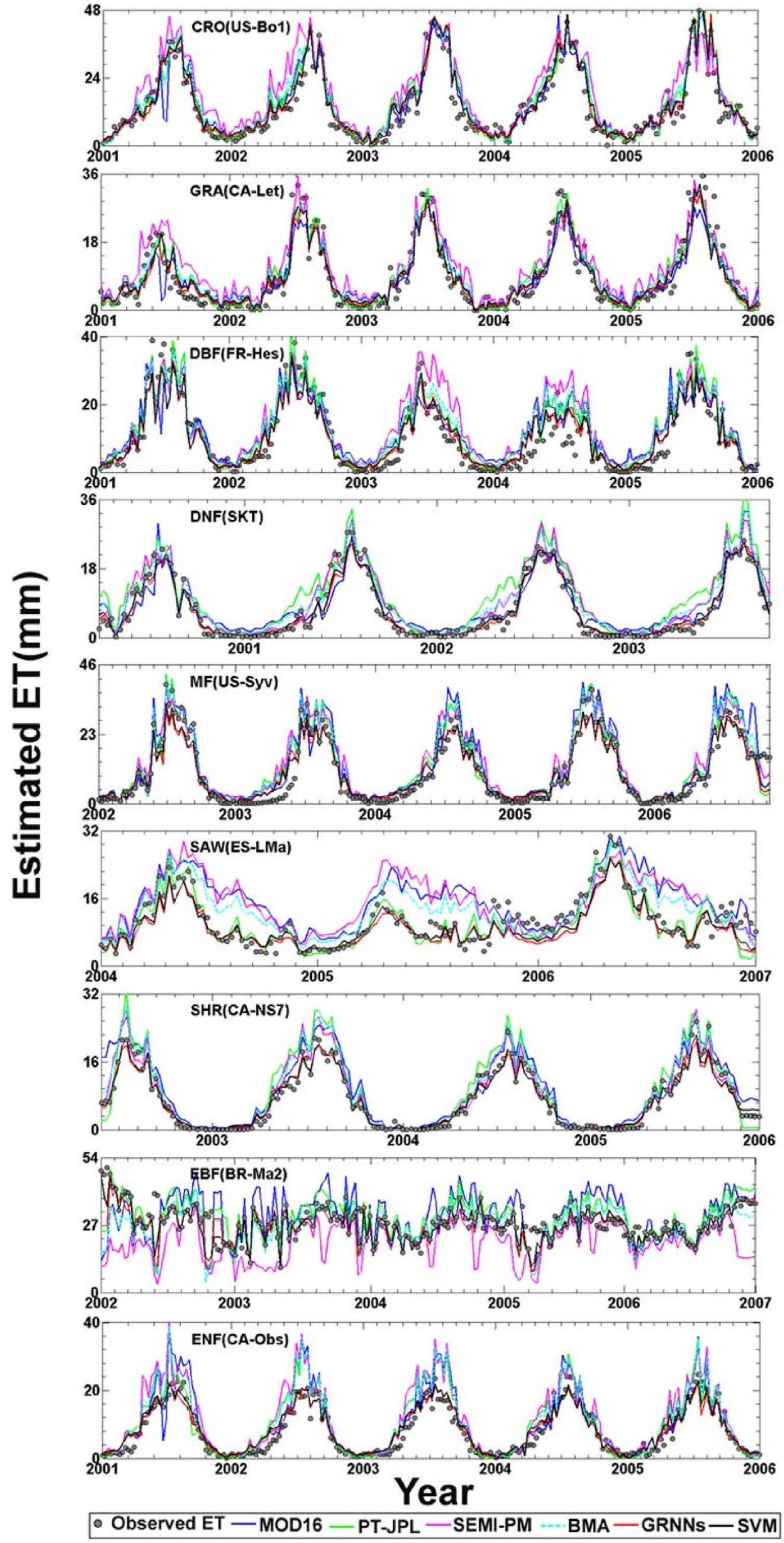

Fig. 6. Examples of the 8-day *ET* average as measured and estimated using the different tower-driven algorithms for the different *PFTs*.

SVM method successfully improved the *ET* estimate accuracy by 10–20% and 5–10% compared with the individual models and other ensemble methods (*BMA* and *GRNNs*), respectively. The *SVM* method performed well and explained more than 81% of the *ET* variability for the *DBF*, *DNF* and *GRA* flux tower sites. Previous studies have shown that the vegetation leaf, moisture and chlorophyll content of these

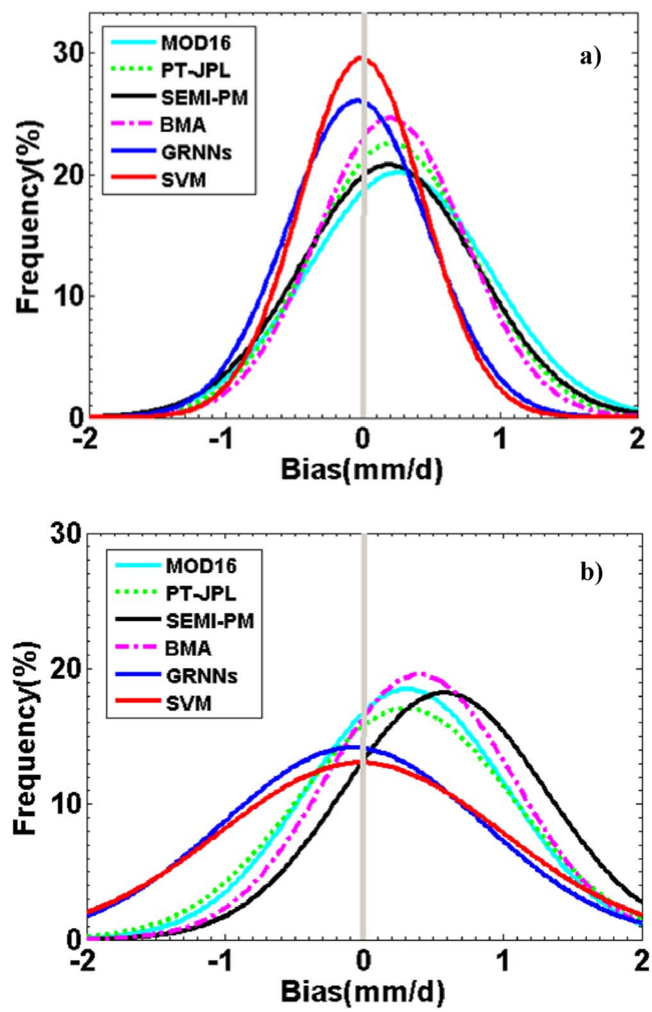

Fig. 7. The frequency distributions of the predictive errors in all six models driven by a) tower-specific and b) *MERRA* meteorology, respectively.

biomes display obviously seasonal variations (Mu et al., 2007; Yao et al., 2015; Yebra et al., 2013). *LAI* and *NDVI* derived from remote sensing reflect the seasonal changes of vegetation information and based on these vegetation parameters, the individual algorithms have successfully captured the seasonal cycle of those biomes, which will improve *ET* estimation because the performance of the *SVM* method relies on the accuracy of the individual algorithms. In contrast to the deciduous forests and grassland cover types, the evergreen forests, including *ENF* and *EBF*, had less evident seasonal variations. Therefore, the weak variations in the satellite-based vegetation signals abated the ability of the individual algorithms and the *SVM* method to calculate *ET* (Eugster et al., 2000; Huete et al., 2002; Wang and Dickinson, 2012). In addition, for the irrigated *CRO* flux tower sites, the *SVM* method presented the poorer local performances for the *ET* (R^2 = 0.51, bias = −0.91 mm/day and *RMSE* = 1.22 mm/day) estimates with *MERRA* meteorology inputs. In contrast, the *SVM* method presented the better local performances for the *ET* (R^2 = 0.60, bias = 0.20 mm/day and *RMSE* = 0.98 mm/day) estimates. This may be attributable to the fact that the *SVM* method failed to simulate irrigation practice because the three satellite-based algorithms only use *RH* and *VPD* to infer soil moisture stress for model parameterization (Fisher et al., 2008; Mu et al., 2011; Wang et al., 2010a). Beyond these irrigated crop sites, the *SVM* method significantly improved the performance.

The relative contributions of each individual algorithm to *SVM*-merged *ET* vary for different *PFTs*. The *SEMI-PM* algorithm has the largest contribution for *DNF*, *ENF* and *MF* land cover types and the *PT-JPL* algorithm has largest contribution for other land cover types, which are generally consistent with the *BMA*-derived weights for the three process-based *ET* algorithms (Fig. 15). The study of Yang (2006) indicated that *SVM* outperformed other techniques (*e.g.* neural networks and multiple regressions) and the contribution of input variable may change with different *PFTs* and spatial resolution. Yao et al. (2014) also reported that *SEMI-PM* latent heat flux estimates had large contribution to *BMA*-merged *ET* for most land cover types because it closely matched the *BMA* latent heat flux estimate.

4.2. SVM-merged global terrestrial ET estimation

The *SVM* method for merging the three process-based *ET* demonstrated its reliability for estimating global terrestrial annual *ET*. Considering that we used the *GRACE* satellite data to compare the *SVM*-based *ET* and the *GRACE* data are available from March 2002, we generated *SVM*-based ET product during period of 2003–2005 in this study. Importantly, the *SVM*-merged annual global terrestrial *ET* (excluding Greenland and Antarctica) was 471.7 mm/yr from 2003 through 2005, which was comparable to other estimates. For instance, Wang and Dickinson (2012) reported that global average *ET* derived from surface water budget varied from 1.2 mm/d to 1.5 mm/d with an average of 1.3 ± 0.1 mm/d. Mueller et al. (2013) inferred that the estimates of globally averaged *ET* from satellite observation, reanalysis data and land surface model simulations were between 0.83 mm/d and 1.45 mm/d. The *SVM* ensemble results were similar to those results. However, spatial differences between the *SVM*-merged *ET* and other *ET* estimates are much greater than those for the global average values. This discrepancy may have been caused by the differences in the algorithm structures of the *SVM* and *GRNNs* methods.

Although the superior performance of the *SVM* method demonstrates that the use of the *SVM* method for merging different *ET* algorithms can effectively characterize the spatial distribution of *ET*, the *SVM* method underestimates monthly *ET* when the measurements exceed 120 mm per month. Similarly, *SVM*-merged averaged *ET* over the tropical and sub-tropical forests is 1279 mm/yr, which was lower than the results of other estimates. For instance, Bruijnzeel (1990) reported that annual *ET* ranges from 1310 to 1500 mm in humid tropical forests. Frank and Inouye (1994) used 25 year climate records to calculate annual *ET* at 10 sites and found annual *ET* of 1363 ± 77 mm/yr for wet tropical forest. Perhaps few training samples available for tropical forest attribute to the underestimate *ET*.

4.3. Uncertainty in SVM-merged ET estimate

Validation results indicate that uncertainty in *SVM*-merged daily *ET* estimate (with respect to *FLUXNET*) was found to range between 21 and 47%. We attribute the reasons for uncertainty in global terrestrial *ET* product to factors such as the corresponding errors in the tower *EC* observations, *MERRA* meteorology and satellite-based vegetation parameters (e.g., *LAI* and *FPAR*) and the spatial scale mismatch among the different data sources. Firstly, the energy balance closure of the *EC* observation was generally approximately 30% due to complexities in the wind patterns and to footprint variability (Foken, 2008; Twine et al., 2000; Wilson et al., 2002; Zhang et al., 2010). Although the *EC* data were corrected, they still had an error of approximately 5–20% (Foken, 2008), which would have reduced the accuracy of the algorithms used for the *ET* estimation. Secondly, many studies have demonstrated that there are large errors in the *MERRA* meteorology and *MERRA* data tend to underestimate R_n at high values when compared with ground measurements (Rienecker et al., 2011; Zhao et al., 2006). This indicates that the biases in *MERRA* meteorological data can introduce substantial uncertainties into the *ET* estimates, and it is necessary to minimize those biases to improve the quality of the *ET* product. Thirdly, the accuracy of the *MODIS LAI*, *FPAR* and land cover types can also influence the accuracy of the *ET* estimates. Recent studies

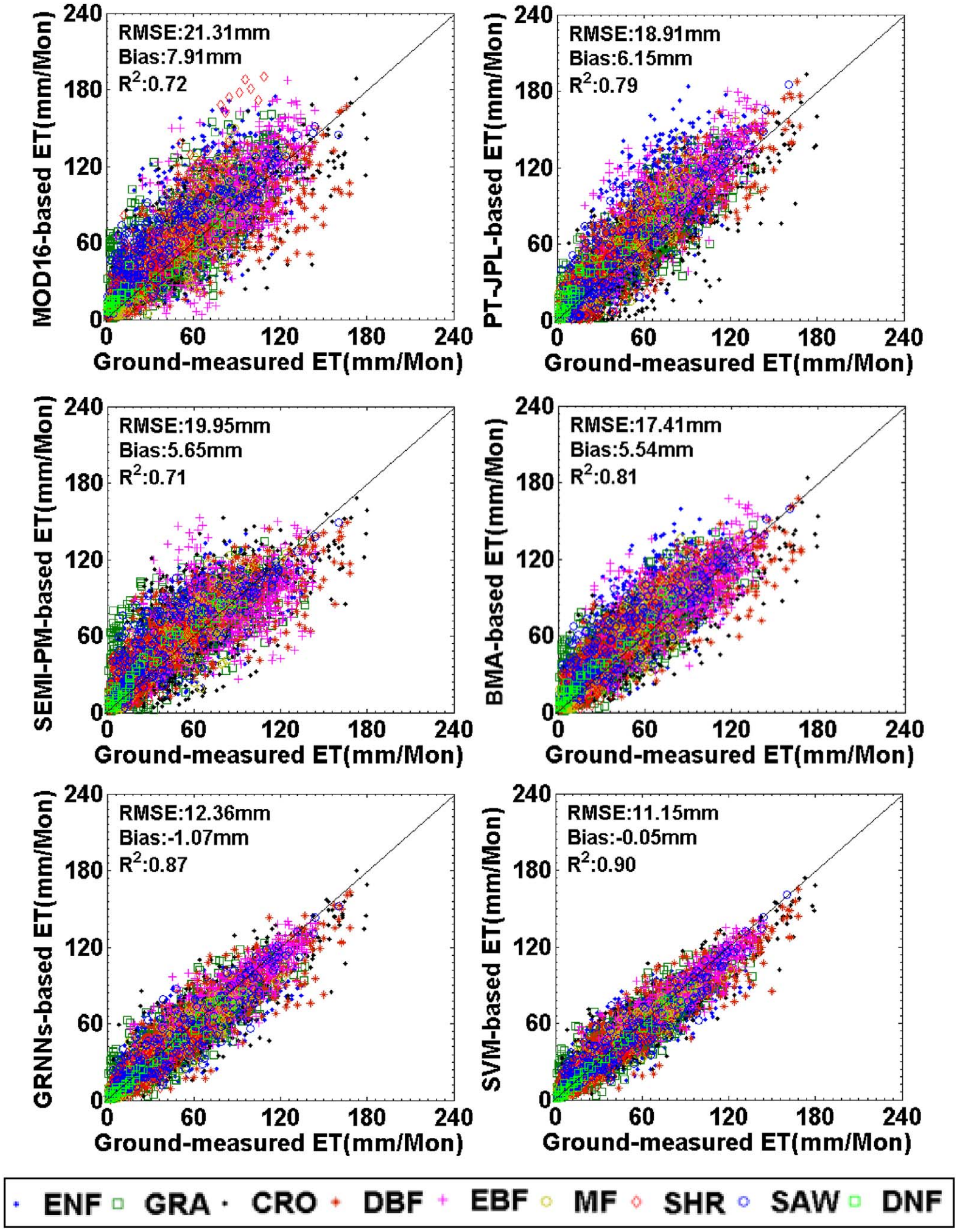

Fig. 8. The scatter plots between the monthly observed *ET* at all 200 flux tower sites and the *ET* estimates for the six algorithms driven by tower-specific meteorology (mm/Mon refers to mm per month).

have revealed errors in *MODIS LAI* and *FPAR* when compared with ground measurements (Serbin et al., 2013). Similarly the accuracy of the *MODIS* Collection 5 Land Cover Type product is less than 75% globally (Hansen et al., 2000), which will lead to approximately 17% errors in *SVM*-merged *ET* estimate. Thus, these inaccurate *MODIS* products will also reduce the accuracy of *ET* estimates. The individual *ET* algorithms, such as *MOD16*, have large errors due to the biases of the *MERRA* and *MODIS* products (Mu et al., 2011; Velpuri et al., 2013). Mu et al. (2011) reported uncertainties in *MOD16 ET* product up to 20% on individual station-based *FLUXNET* validation. Finally, the spatial scale mismatch among the different data sources may have introduced errors in the *ET* estimation. The spatial resolution of the gridded data including the *MERRA* and *MODIS* products, was no less than 1-km, which was greater than the footprint for field measurements, which have spatial resolutions of several meters (Baldocchi, 2008). Such coarse *MERRA* and *MODIS* products may not adequately capture sub-grid scale meteorological and vegetation signals at these sites, especially in areas with complex land surfaces.

The performance of the *SVM*-merged *ET* estimates was not only validated at the site scale but was also evaluated at the basin scale using water balance approach. Basin scale validation results indicated uncertainties up to 21% of the annual estimates for *SVM*-merged *ET*. The accuracy of the inferred *ET* using water balance approach could be also affected by the sources of error in *P*, *Q* and *TWSC*. Pan et al. (2012) reported that about 10% relative error in both *P* and *Q* will persist at 15 per 10^6 km^2 despite increasing gauge density. The error in *TWSC* caused by the different methods for *GRACE* estimation (Swenson and Wahr, 2002) can lead to 14% error in calculated *ET* using water balance approach. In addition, the spatial resolution of *MODIS* products was approximately 5 km in size and was much finer than the resolution

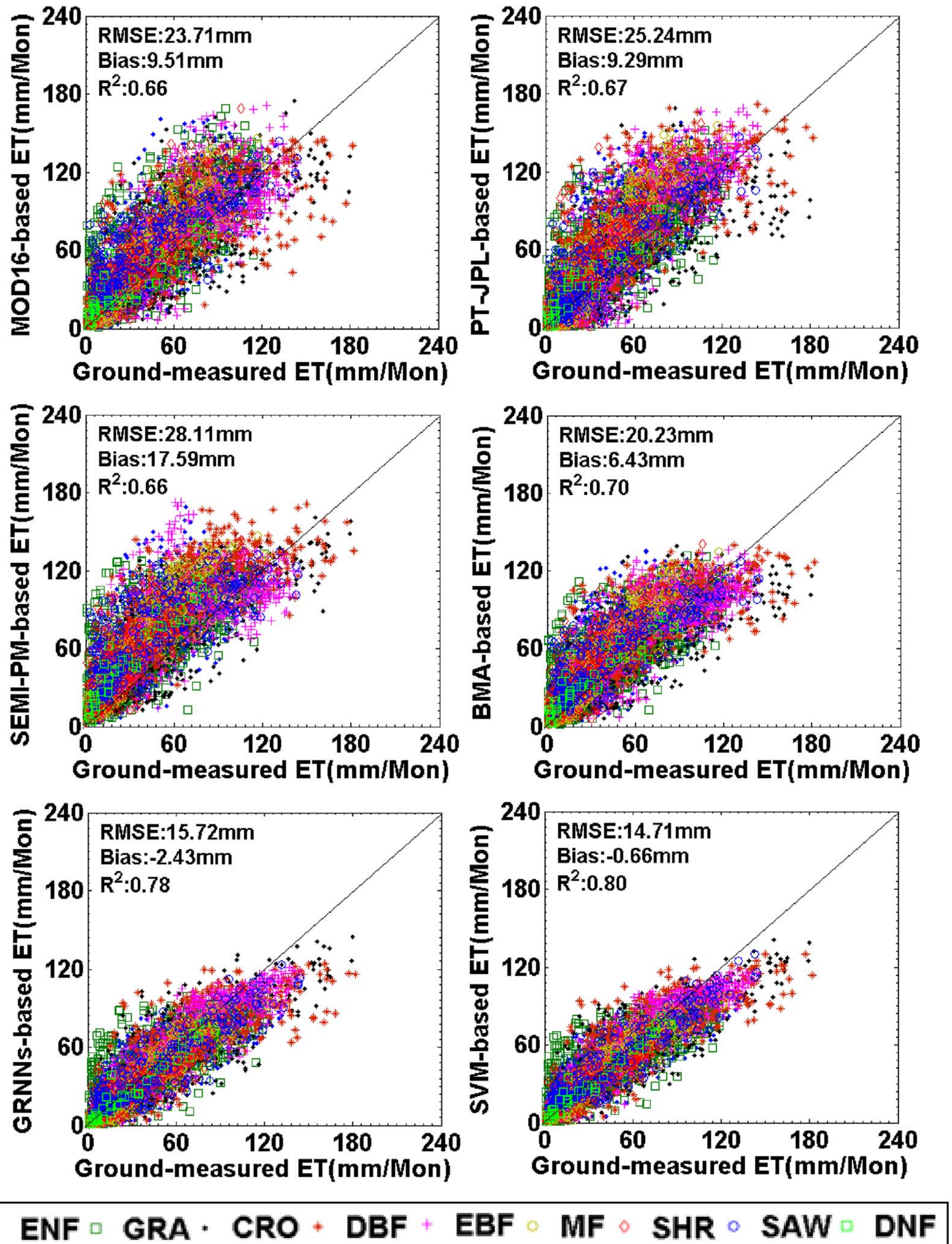

Fig. 9. The scatter plots between the monthly observed *ET* at all 200 flux tower sites and the *ET* estimates for the six algorithms driven by *MERRA* meteorology (mm/Mon refers to mm per month).

(more than 50 km) of other gridded products including *MERRA*, *GRACE*, fused *P* and *Q* datasets. Although all gridded products were interpolated into 5 km, error propagation through calculations, including threshold filtering, averaging, interpolation, and data fusion affected the uncertainty of the comparison of the *SVM*-merged *ET* and inferred *ET* based on water balance approach. Even if all the errors could be eliminated from a model and even if observational uncertainties could be reduced to zero, the modeled and observed estimates cannot be expected to be identical (Taylor, 2001). Therefore, the choice of a reasonable dataset should be made carefully depending on the requirements of the study.

4.4. Limitations and recommendations for future research

Although the *SVM* highlights global rather than local optima and leads to better performance compared with other machine learning methods, such as the *GRNNs* method, which ensures local optimization (Shrestha and Shukla, 2015; Specht, 1991; Vapnik, 1995; Verrelst et al., 2015; Yang, 2006), it faces three known limitations. Firstly, it requires a relatively long processing time (about 47.3 s for 1000 samples) to train a model. Secondly, it behaves relatively unpredictable when used with input ground-measured *ET* deviating from those presented during the training stage (Shrestha and Shukla, 2015; Verrelst et al., 2012). Finally, regardless of the performance outcome, however, we do not know that any of machine learning methods possess the useful information to directly deliver additional confidence *ET* maps. Confidence *ET* maps should be evaluated and validated using other ground-measured *ET* data from other *PFTs EC* sites.

To make the training samples more globally applicable, it is urgent to add samples from other *PFTs* (*e.g.* snow and ice). However, there are

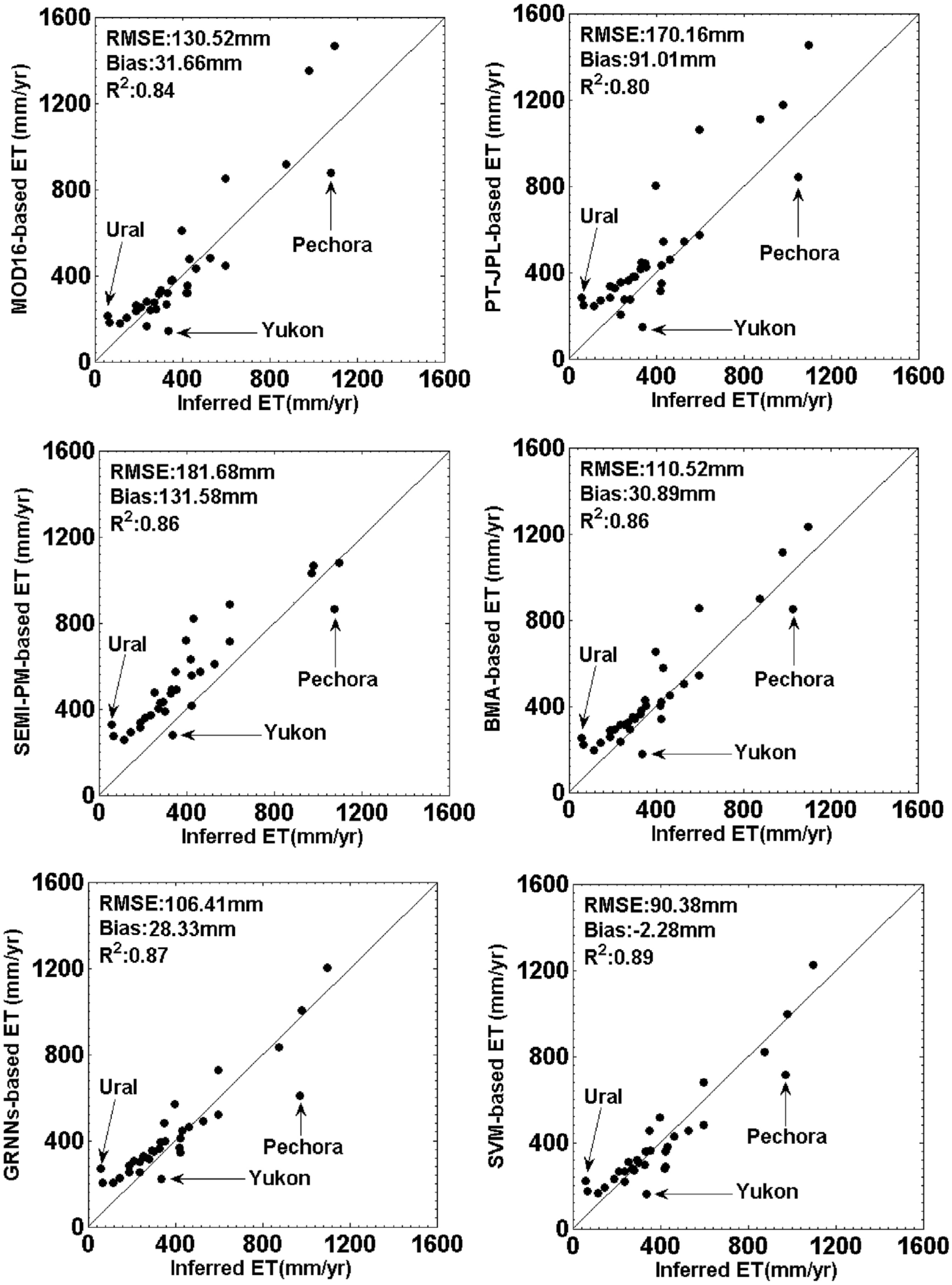

Fig. 10. Comparison of the estimated *ET* using six algorithms driven by *MERRA* meteorology and the corresponding *ET* inferred by the water balance equation over the global 32 river basins.

few *EC* data available for these specific *PFTs*. During the past decades, there are many semi-empirical and physical methods for estimating the sublimation of snow and ice (Kuzmin, 1953; Hu and Jia, 2015). The advantage of these methods is that they do not require training samples to estimate the sublimation of snow and ice, though the accuracy of these methods may not be the highest. Future research will consider the development of machine learning methods when coupled with these semi-empirical and physical methods to improve the global terrestrial *ET* at more different *PFTs*.

5. Conclusions

We used the *SVM* method to merge three satellite-based *ET* algorithms (*MOD16*, *PT-JPL* and *SEMI-PM*) for global terrestrial *ET* estimation across multiple biomes. The inputs of each algorithm included tower-specific meteorology collected from 200 global flux tower sites, *MERRA* meteorology and *MODIS* products. Compared to the *BMA* method, the *GRNNs* method and the individual algorithms, the *SVM* methods had the best performance for each vegetation type and can be effectively applied to estimate global terrestrial *ET*.

The performance of the *SVM* method was examined at 200 *FLUXNET EC* flux towers based on a fourfold cross-validation method for each *PFT*. The *SVM* method enhanced *ET* estimates by merging the three satellite-based *ET* algorithms driven by tower-specific (*MERRA*) meteorology, decreasing the tower-specific *RMSE* of the daily *ET* by approximately 0.20 (0.15) mm/day for most of the forest sites and by

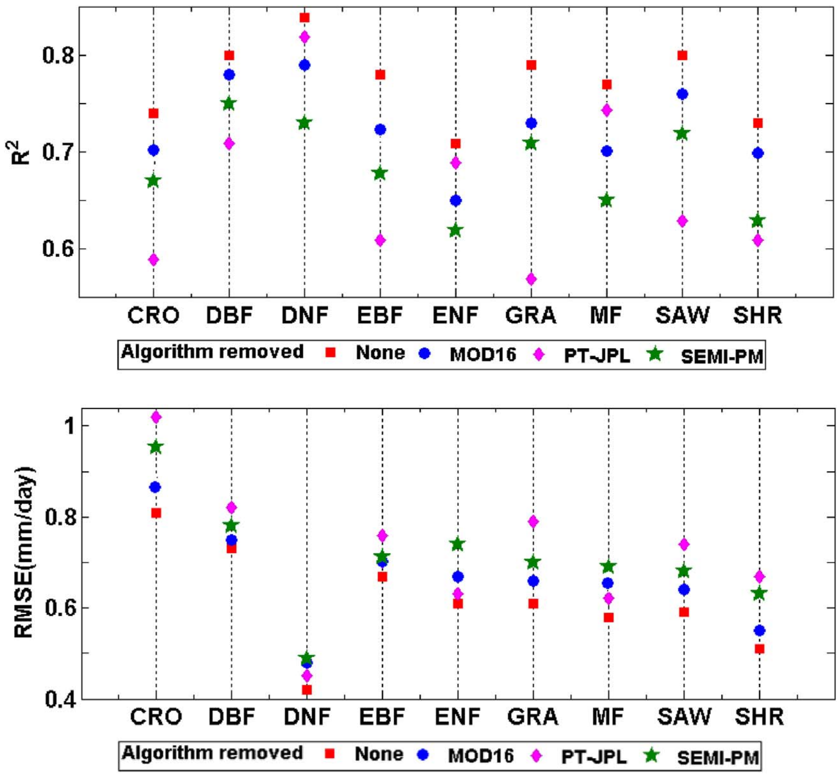

Fig. 11. Impact of removing one of the three algorithms on the predicting performance (R^2 and *RMSE*) of *SVM* on *ET*. The results shown are the average from a fourfold cross-validation on the training data.

approximately 0.39 (0.20) mm/day for most of the crop and grass sites. The *SVM*-merged *ET* estimates captured the magnitudes of the *ET* measurements better than the *BMA* method, the *GRNNs* method and the individual algorithms. The regional water balance analysis also demonstrated that the regional estimates of the ensemble *ET* were reliable.

The *SVM* method improved annual *ET* estimates by merging the three satellite-based *ET* algorithms driven by *MERRA* meteorology and *MODIS* products. The mean annual *SVM*-merged *ET* over the global terrestrial ecosystem during 2003–2005 was 471.7 mm/yr, which was closer to the observations than that produced by the algorithms

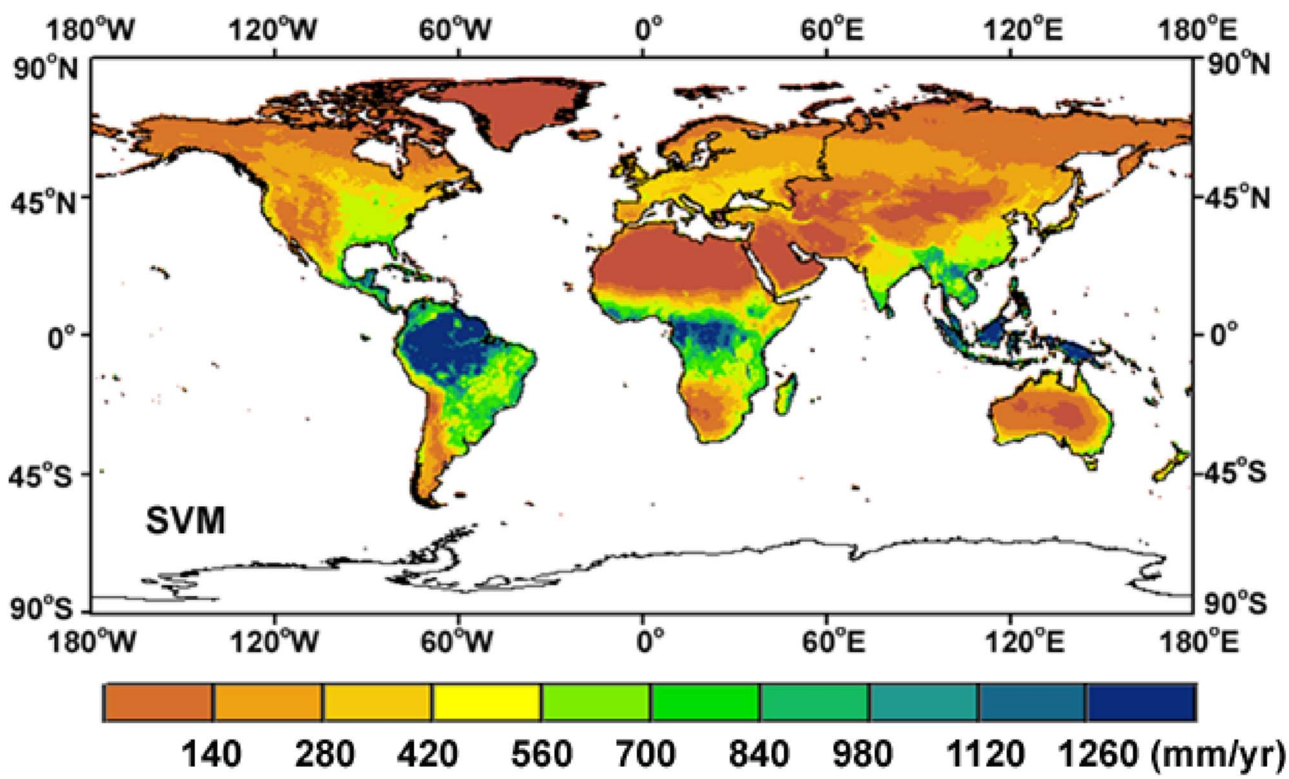

Fig. 12. The map of mean annual global terrestrial *ET* from 2003 through 2005 at a spatial resolution of 0.05° using different algorithms driven by *MERRA* meteorology.

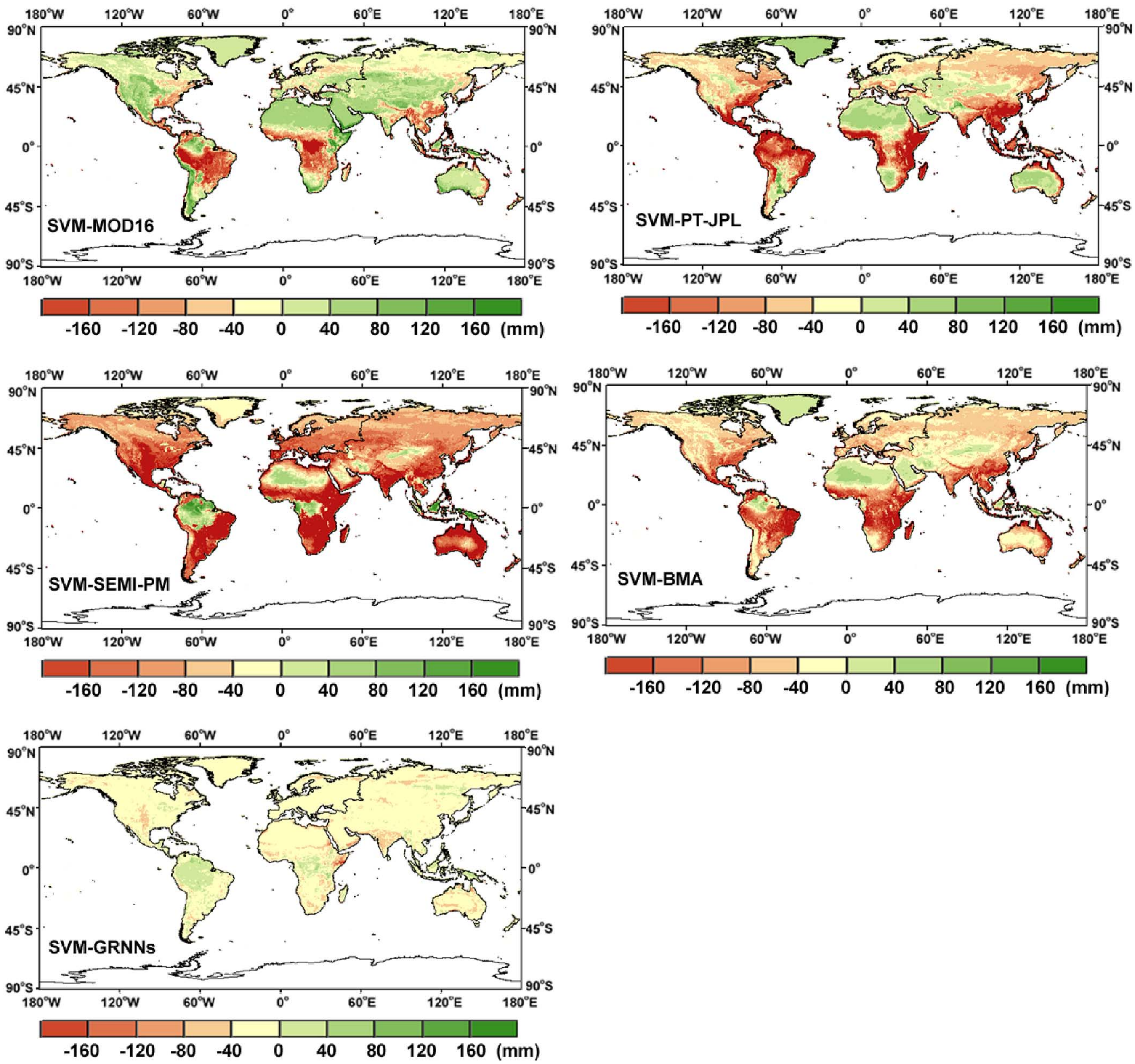

Fig. 13. Spatial differences in the average annual global terrestrial *ET* (2003–2005) between the *SVM* method and other models.

individually. More importantly, the *SVM*-merged *ET* will provide critical information for the characterization of global terrestrial water and energy cycles as well as regional drought assessment.

Acknowledgements

We would like to thank Dr. Tongren Xu and Dr. Ziwei Xu from Beijing Normal University, China, and Prof. Guangsheng Zhou from the Institute of Botany, *CAS*, and Dr. Yan Li and Dr. Ran Liu from Xinjiang Institute of Ecology and Geography, *CAS*, and Prof. Guoyi Zhou and Dr. Yuelin Li from South China Botanic Garden, *CAS*, and Prof. Bin Zhao from Fudan University, China, for providing ground-measured data. This work used eddy covariance data acquired by the FLUXNET community and in particular by the following networks: AmeriFlux (U.S. Department of Energy, Biological and Environmental Research, Terrestrial Carbon Program (DE-FG02-04ER63917 and DE-FG02-04ER63911)), AfriFlux, AsiaFlux, CarboAfrica, CarboEuropeIP, CarboItaly, CarboMont,ChinaFlux, Fluxnet-Canada (supported by CFCAS, NSERC, BIOCAP, Environment Canada, and NRCan), GreenGrass, KoFlux, LBA, NECC, OzFlux, TCOS-Siberia, USCCC. We acknowledge the financial support to the eddy covariance data harmonization provided by CarboEuropeIP, FAO-GTOS-TCO, iLEAPS, Max Planck Institute for Biogeochemistry, National Science Foundation, University of Tuscia, Université Laval, Environment Canada and US Department of Energy and the database development and technical support from Berkeley Water Center, Lawrence Berkeley National Laboratory, Microsoft Research eScience, Oak Ridge National Laboratory, University of California-Berkeley and the University of Virginia. Other ground-measured data were obtained from the *GAME AAN* (http://aan.suiri.tsukuba.ac.jp/), the Arid/Semi-arid experimental observation synergy and integration of northern China (http://observation.tea.ac.cn/), and the water experiments of Environmental and Ecological Science Data Center for West China (http://westdc.westgis.ac.cn/water). *GRACE* product was downloaded online (http://grace.jpl.nas a.gov/). *MODIS LAI/FPAR*, *NDVI* and land cover satellite products were obtained online (http://reverb.echo.nasa.gov/reverb).

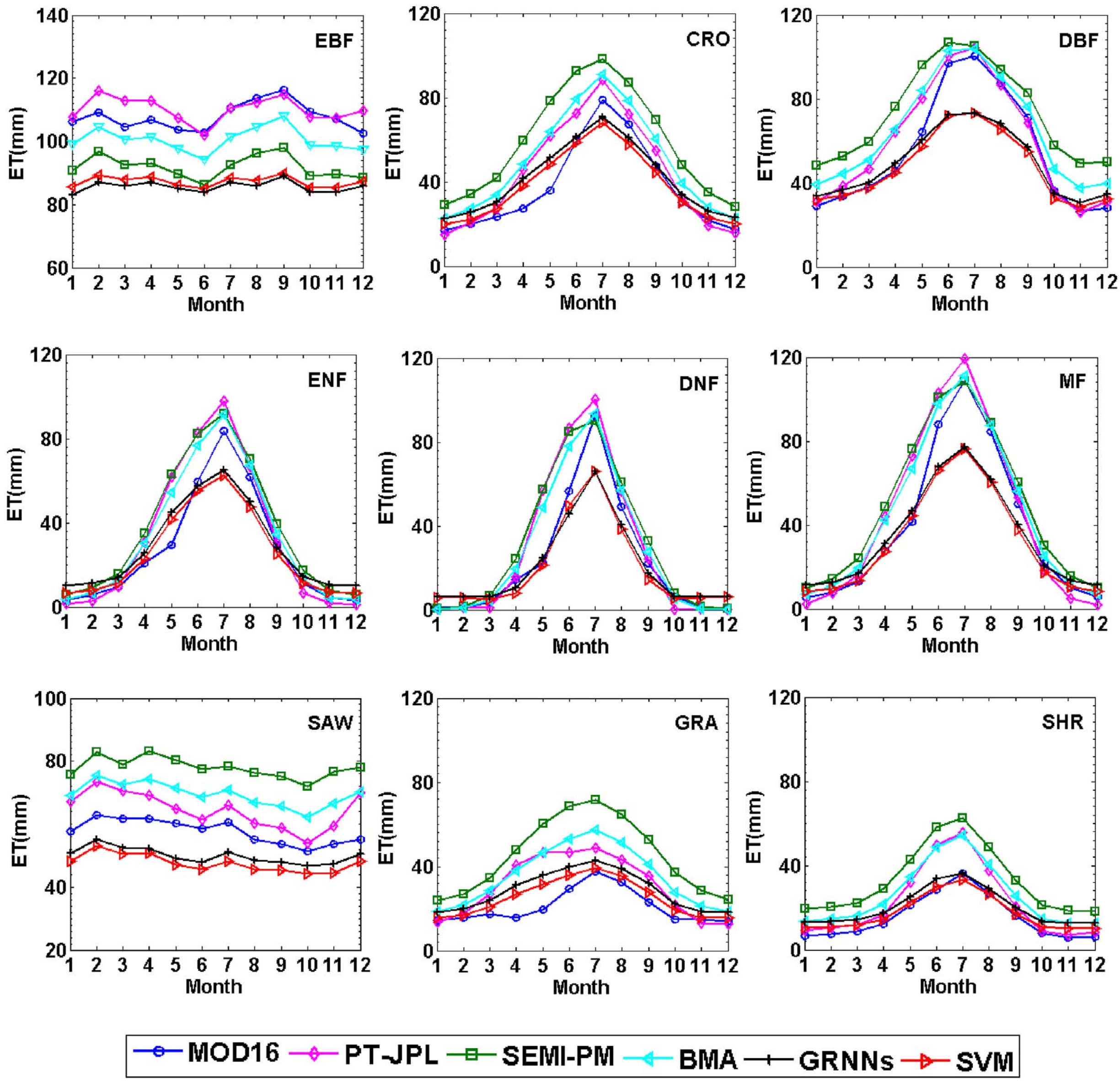

Fig. 14. The seasonality in averaged *SVM*-merged *ET* (2003–2005) at the nine *PFTs*.

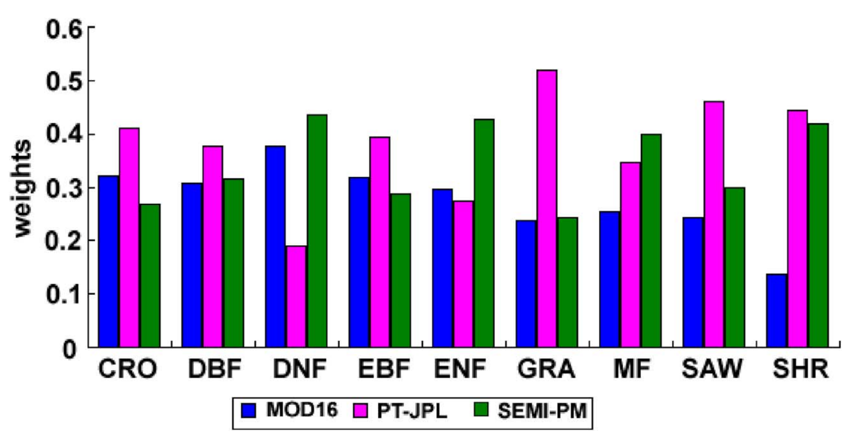

Fig. 15. Weights of the *BMA* method for three satellite-based algorithms driven by tower-specific meteorology.

This work was partially supported by the Natural Science Fund of China (No. 41671331) and the National Key Research and Development Program of China (No.2016YFA0600102 and No. 2016YFB0501404).

References

Akaike, H., 1974. A new look at the statistical model identification. IEEE Trans. Automat. Contr. 19, 716–723.

Allen, R.G., Pereira, L.S., Raes, D., Smith, M., 1998. Crop Evapotranspiration: Guidelines for Computing Crop Requirements, FAO Irrigation and Drainage Paper 56. Food and Agricultural Organization of the U.N., Rome.
Allen, R., Tasumi, M., Trezza, R., 2007. Satellite-based energy balance for mapping evapotranspiration with internalized calibration (METRIC)-Model. J. Irig. Drain. E-ASCE 133, 380–394.
Anderson, M., Norman, M., Diak, G., Kustas, W., Mecikalski, J., 1997. A two-source time-integrated model for estimating surface fluxes using thermal infrared remote sensing. Remote Sens. Environ. 60, 195–216.
Baldocchi, D., 2008. Breathing of the terrestrial biosphere: lessons learned from a global network of carbon dioxide flux measurement systems. Aust. J. Bot. 56, 1–26.
Bastiaanssen, W., Menenti, M., Feddes, R., Holtslag, A., 1998. A remote sensing surface energy balance algorithm for land (SEBAL): 1. Formulation. J. Hydrol. 212, 198–212.
Bruijnzeel, L.A., 1990. Hydrology of Moist Tropical Forests and Effects of Conversion: A State of Knowledge Review, International Hydrological Programme. UNESCO, Paris, France.
Chen, Y., et al., 2015. Using Bayesian model averaging to estimate terrestrial evapotranspiration in China. J. Hydrol. 528, 537–549.
Cleugh, H.A., Leuning, R., Mu, Q., Running, S., 2007. Regional evaporation estimates from flux tower and MODIS satellite data. Remote Sens. Environ. 106, 285–304.
Dibike, Y., Velickov, S., Solomatine, D., Abbott, M., 2001. Model induction with support vector machines: introduction and applications. J. Comput. Civ. Eng. 15, 208–216.
Duan, Q., Phillips, T.J., 2010. Bayesian estimation of local signal and noise in multimodel simulations of climate change. J. Geophys. Res. Atmos. 115, D18123.
Eugster, W., et al., 2000. Land-atmosphere energy exchange in Arctic tundra and boreal forest: available data and feedbacks to climate. Global Change Biol. 6, 84–115.
Fisher, J.B., Tu, K.P., Baldocchi, D.D., 2008. Global estimates of the land atmosphere water flux based on monthly AVHRR and ISLSCP-II data, validated at 16 FLUXNET sites. Remote Sens. Environ. 112, 901–919.
Foken, T., 2008. The energy balance closure problem. An overview. Ecol. Appl. 18, 1351–1367.
Frank, D.A., Inouye, R.S., 1994. Temporal variation in actual evapotranspiration of terrestrial ecosystems-patterns and ecological implications. J. Biogeogr. 21, 401–411.
Friedl, M.A., et al., 2002. Global land cover mapping from MODIS: Algorithms and early results. Remote Sens. Environ. 83, 287–302.
Friedl, M.A., 1996. Relationships among remotely sensed data, surface energy balance, and area-averaged fluxes over partially vegetated land surfaces. J. Appl. Meteor. 35, 2091–2103.
Hansen, M., Defries, R., Townshend, J., Sohlberg, R., 2000. Global land cover classification at 1 km spatial resolution using a classification tree approach. Int. J. Remote Sens. 21, 1331–1364.
Hu, G., Jia, L., 2015. Monitoring of evapotranspiration in a semi-arid inland river basin by combining microwave and optical remote sensing observations. Remote Sens. 7, 3056–3087.
Huete, A., Didan, K., Miura, T., Rodriguez, E.P., Gao, X., Ferreira, L.G., 2002. Overview of the radiometric and biophysical performance of the MODIS vegetation indices. Remote Sens. Environ. 83, 195–213.
Jackson, R., Reginato, R., Idso, S., 1977. Wheat canopy temperature: a practical tool for evaluating water requirements. Water Resour. Res. 13, 651–656.
Jia, K., et al., 2015. Global Land surface fractional vegetation cover estimation using general regression neural networks from MODIS surface reflectance. IEEE Trans. Geosci. Remote Sens. 9, 4787–4796.
Jia, Z., Liu, S., Xu, Z., Chen, Y., Zhu, M., 2012. Validation of remotely sensed evapotranspiration over the Hai River Basin, China. J. Geophys. Res. Atmos. 117, D13113.
Jiménez, C., et al., 2011. Global intercomparison of 12 land surface heat flux estimates. J. Geophys. Res. Atmos. 116, D02102.
Jung, M., et al., 2010. Recent decline in the global land evapotranspiration trend due to limited moisture supply. Nature 467, 951–954.
Jung, M., et al., 2011. Global patterns of land-atmosphere fluxes of carbon dioxide, latent heat, and sensible heat derived from eddy covariance, satellite, and meteorological observations. J. Geophys. Res. Atmos. 116, G00J07.
Khalil, A.F., McKee, M., Kemblowski, M., Asefa, T., Bastidas, L., 2006. Multiobjectiveanalysis of chaotic dynamic systems with sparse learning machines. Adv. Water Resour. 29, 72–88.
Korzoun, V.I., Sokolov, A.A., Budyko, M.I., Voskresensky, K.P., Kalinin, G.P., 1978. World Water Balance and Water Resources of the Earth (English). Studies and Reports in Hydrology (UNESCO), No. 25/United Nations Educational, Scientific and Cultural Organization 75 International Hydrological Decade. Moscow (USSR): USSR National Committee, Paris (France) (663 p).
Kustas, W., Daughtry, C., 1990. Estimation of the soil heat-flux net-radiation ratio from spectral data. Agric. For. Meteorol. 49, 205–223.
Kuzmin, P.P., 1953. On method for investigations of evaporation from the snow cover. Trans. State Hydrol. Inst. 41, 34–52 (In Russian).
Liang, S., Wang, K., Zhang, X., Wild, M., 2010. Review on estimation of land surface radiation and energy budgets from ground measurement, remote sensing and model simulations. IEEE J. Sel. Top. Appl. Earth Obs. Remote Sens. 3, 225–240.
Liang, S., et al., 2013. A long-term global land surface satellite (GLASS) dataset for environmental studies. Int. J. Digit. Earth. 6, 5–33.
Liu, S., Xu, Z., Wang, W., Jia, Z., Zhu, M., Bai, J., Wang, J., 2011. A comparison of eddy-covariance and large aperture scintillometer measurements with respect to the energy balance closure problem. Hydrol. Earth Syst. Sci. 15, 1291–1306.
Liu, S., Xu, Z., Zhu, Z., Jia, Z., Zhu, M., 2013. Measurements of evapotranspiration from eddy-covariance systems and large aperture scintillometers in the Hai River Basin, China. J. Hydrol. 487, 24–38.
Loehlin, J.C., 1992. Latent Variable Models: an Introduction to Factor, Path, and Structural Analysis. Hillsdale, NJ: Erlbaum.
Los, S.O., et al., 2000. A global 9-yr biophysical land surface dataset from NOAA AVHRR data. J. Hydrometeorol. 1, 183–199.
Lu, X., Zhuang, Q., 2010. Evaluating evapotranspiration and water-use efficiency of terrestrial ecosystems in the conterminous United States using MODIS and AmeriFlux data. Remote Sens. Environ. 114, 1924–1939.
McVicar, T.R., et al., 2012. Global review and synthesis of trends in observed terrestrial near-surface wind speeds: implications for evaporation. J. Hydrol. 416-417, 182–205.
Mu, Q., Heinsch, F., Zhao, M., Running, S., 2007. Development of a global evapotranspiration algorithm based on MODIS and global meteorology data. Remote Sens. Environ. 111, 519–536.
Mu, Q., Zhao, M., Running, S., 2011. Improvements to a MODIS global terrestrial evapotranspiration algorithm. Remote Sens. Environ. 115, 1781–1800.
Mueller, B., et al., 2013. Benchmark products for land evapotranspiration: landFlux-EVAL multi-data set synthesis. Hydrol. Earth Syst. Sci. 17, 3707–3720.
Myneni, R., et al., 2002. Global products of vegetation leaf area and fraction absorbed PAR from year one of MODIS data. Remote Sens. Environ. 83, 214–231.
National Research Council, 2007. Earth Science and Applications From Space: National Imperatives for the Next Decade and Beyond. Natl. Acad. Press, Washington, D. C (400 pp).
Norman, J., Kustas, W., Humes, K., 1995. Source approach for estimating soil and vegetation energy fluxes in observations of directional radiometric surface temperature. Agric. For. Meteorol. 77, 263–293.
Nurmemet, I., et al., 2015. Monitoring soil salinization in Keriya river basin, northwestern China using passive reflective and active microwave remote sensing data. Remote Sens. 7, 8803–8829.
Pan, M., Sahoo, A.K., Troy, T.J., Vinukollu, R.K., Sheffield, J., Wood, E.F., 2012. Multisource estimation of long-term terrestrial water budget for major global river basins. J. Clim. 25, 3191–3206.
Penman, H.L., 1948. Natural evaporation from open water bare soil and grass. Proc. R. Soc. London Ser. A 193, 120–145.
Pipunic, R., Walker, J., Western, A., 2008. Assimilation of remotely sensed data for improved latent and sensible heat flux prediction. A comparative synthetic study. Remote Sens. Environ. 112, 1295–1305.
Priestley, C., Taylor, R., 1972. On the assessment of surface heat flux and evaporation using large-scale parameters. Mon. Weather Rev. 100, 81–92.
Raftery, A.E., Gneiting, T., Balabdaoui, F., Polakowski, M., 2005. Using bayesian model averaging to calibrate forecast ensembles. Mon. Weather Rev. 113, 1155–1174.
Rienecker, M., et al., 2011. MERRA-NASA's modern-era retrospective analysis for research and applications. J. Clim. 24, 3624–3648.
Schwarz, G., 1978. Estimating the dimension of a model. Ann. Statist. 6, 461–464.
Serbin, S., Ahl, D., Gower, S., 2013. Spatial and temporal validation of the MODIS LAI and FPAR products across a boreal forest wildfire chronosequence. Remote Sens. Environ. 133, 71–84.
Sheffield, J., Wood, E., 2008. Projected changes in drought occurrence under future global warming from multi-model, multi-scenario, IPCC AR4 simulations. Clim. Dyn. 31, 79–105.
Shrestha, N., Shukla, S., 2015. Support vector machine based modeling of evapotranspiration using hydro-climatic variables in a sub-tropical environment. Agric. For. Meteorol. 200, 172–184.
Specht, D.F., 1991. A general regression neural network. IEEE Trans. Neural Netw. 2, 568–576.
Su, Z., 2002. The surface energy balance system (SEBS) for estimation of turbulent heat fluxes. Hydrol. Earth Syst. Sci. 6, 85–100.
Swenson, S., Wahr, J., 2002. Methods for inferring regional surface-mass anomalies from Gravity Recovery and Climate Experiment (GRACE) measurements of time-variable gravity. J. Geophys. Res. Atmos. 107, 2193.
Taylor, K., 2001. Summarizing multiple aspects of model performance in a single diagram. J. Geophys. Res. Atmos. 106, 7183–7192.
Tramontana, G., et al., 2016. Predicting carbon dioxide and energy fluxes across global FLUXNET sites with regression algorithms. Biogeosciences 13, 4291–4313.
Twine, T.E., Kustas, W.P., Norman, J.M., Cook, D.R., Houser, P.R., Meyers, T.P., Prueger, J.H., Starks, P.J., Wesely, M.L., 2000. Correcting eddy covariance flux underestimates over a grassland. Agric. For. Meteorol. 103, 279–300.
Vapnik, V.N., 1995. The Nature of Statistical Learning Theory. Springer Verlag, NewYork.
Velpuri, N.M., Senay, G.B., Singh, R.K., Bohms, S., Verdin, J.P., 2013. A comprehensive evaluation of two MODIS evapotranspiration products over the conterminous United States Using point and gridded FLUXNET and water balance ET. Remote Sens. Environ. 139, 35–49.
Verrelst, J., Muñoz, J., Alonso, L., Delegido, J., Rivera, J.P., Camps-Valls, G., Moreno, J., 2012. Machine learning regression algorithms for biophysical parameter retrieval Opportunities for Sentinel-2 and −3. Remote Sens. Environ. 118, 127–139.
Verrelst, J., Rivera, J.P., Veroustraete, F., Muñoz-Marí, J., Clevers, Jan G.P.W., Camps-Valls, G., Moreno, J., 2015. Experimental Sentinel-2 LAI estimation using parametric, non-parametric and physical retrieval methods-A comparison. ISPRS J. Photogramm. 108, 260–272.
Wang, K., Dickinson, R., 2012. A review of global terrestrial evapotranspiration: observation, modeling, climatology, and climatic variability. Rev. Geophys. 50, RG2005.
Wang, K., Liang, S., 2008. An improved method for estimating global evapotranspiration based on satellite determination of surface net radiation, vegetation index, temperature, and soil moisture. J. Hydrometeorol. 9, 712–727.
Wang, K., Wang, P., Li, Z.Q., Cribb, M., Sparrow, M., 2007. A simple method to estimate actual evapotranspiration from a combination of net radiation, vegetation index, and temperature. J. Geophys. Res. Atmos. 112, D15107.
Wang, K., Dickinson, R.E., Wild, M., Liang, S., 2002a. Evidence for decadal variation in

global terrestrial evapotranspiration between 1982 and 2002: 1. Model development. J. Geophys. Res. Atmos. 115, D20112.
Wang, K., Dickinson, R.E., Wild, M., Liang, S., 2002b. Evidence for decadal variation in global terrestrial evapotranspiration between 1982 and 2002: 2. Results. J. Geophys. Res. Atmos. 115, D20113.
Wilson, K., et al., 2002. Energy balance closure at FLUXNET sites. Agric. For. Meteorol. 113, 223–243.
Wu, H., Zhang, X., Liang, S., Yang, H., Zhou, G., 2012. Estimation of clear-sky land surface longwave radiation from MODIS data products by merging multiple models. J. Geophys. Res. Atmos. 117, D22107.
Xiao, Z., et al., 2014. Use of general regression neural networks for generating the GLASS leaf area index product from time-series MODIS surface reflectance. IEEE Trans. Geosci. Remote Sens. 52, 209–223.
Xu, T., Liang, S., Liu, S., 2011a. Estimating turbulent fluxes through assimilation of geostationary operational environmental satellites data using ensemble Kalman filter. J. Geophys. Res. Atmos. 116, D09109.
Xu, T., Liu, S., Liang, S., Qin, J., 2011b. Improving predictions of water and heat fluxes by assimilating MODIS land surface temperature products into common land model. J. Hydrometeorol. 12, 227–244.
Xu, Z., Liu, S., Li, X., Shi, S., Wang, J., Zhu, Z., Xu, T., Wang, W., Ma, M., 2013. Intercomparison of surface energy flux measurement systems used during the HiWATER-MUSOEXE. J. Geophys. Res. Atmos. 118, 13140–13157.
Yang, F., 2006. Prediction of continental-scale evapotranspiration by combining MODIS and AmeriFlux data through support vector machine. IEEE Trans. Geosci. Remote Sens. 44, 3452–3461.
Yao, Y., et al., 2013. MODIS-driven estimation of terrestrial latent heat flux in China based on a modified Priestly-Taylor algorithm. Agric. For. Meteorol. 171, 187–202.
Yao, Y., et al., 2014. Bayesian multimodel estimation of global terrestrial latent heat flux from eddy covariance, meteorological, and satellite observations. J. Geophys. Res. Atmos. 119, 4521–4545.
Yao, Y., Liang, S., Li, X., Chen, J., Wang, K., Jia, K., Cheng, J., Jiang, B., Fisher, J.B., Mu, Q., Grünwald, T., Bernhofer, C., Roupsard, O., 2015. A satellite-based hybrid algorithm to determine the Priestley-Taylor parameter for global terrestrial latent heat flux estimation across multiple biomes. Remote Sens. Environ. 165, 216–233.
Yao, Y., et al., 2016. Assessment and simulation of global terrestrial latent heat flux by synthesis of CMIP5 climate models and surface eddy covariance observations. Agric. For. Meteorol. 223, 151–167.
Yebra, M., Van Dijk, A., Leuning, R., Huete, A., Guerschman, J., 2013. Evaluation of optical remote sensing to estimate actual evapotranspiration and canopy conductance. Remote Sens. Environ. 129, 250–261.
Yuan, Y., et al., 2010. Global estimates of evapotranspiration and gross primary production based on MODIS and global meteorology data. Remote Sens. Environ. 114, 1416–1431.
Zhang, K., Kimball, J., Nemani, R., Running, S., 2010. A continuous satellite-derived global record of land surface evapotranspiration from 1983 to 2006. Water Resour. Res. 46, W09522.
Zhao, M., Heinsch, F.A., Nemani, R., Running, S.W., 2005. Improvements of the MODIS terrestrial gross and net primary production global data set. Remote Sens. Environ. 95, 164–176.
Zhao, M., Running, S., Nemani, R., 2006. Sensitivity of Moderate Resolution Imaging Spectroradiometer (MODIS) terrestrial primary production to the accuracy of meteorological reanalysis. J. Geophys. Res. Atmos. 111, G01002.